

# Distinguishing Beyond-Standard Model Effects in Neutrino Oscillation

A. Calatayud-Cadenillas,<sup>1,\*</sup> A. Pérez-G.,<sup>1,†</sup> and A. M. Gago<sup>1,‡</sup>

<sup>1</sup>*Sección Física, Departamento de Ciencias,  
Pontificia Universidad Católica del Perú, Apartado 1761, Lima, Perú*

We systematically assess the DUNE experiment’s ability to distinguish between various beyond-standard neutrino oscillation hypotheses pair combinations. For a pair comparison, we evaluate the statistical separation, where one hypothesis plays the role of the true signal while the other corresponds to the test signal. The beyond-standard neutrino oscillation hypotheses under scrutiny include neutrino decay (invisible and visible), non-standard interactions, quantum decoherence, and the violation of the equivalence principle. When taken as the true model, we found that either quantum decoherence or the violation of the equivalence principle are the easiest to differentiate compared to the rest of the hypotheses. Additionally, from our statistical test, we investigate potential discrepancies between the measured CP-violation phase  $\delta_{CP}$  relative to its true value, which could occur for a given comparison. In our analysis, we will take the true values of  $\delta_{CP}$  as  $-90^\circ$  and  $180^\circ$ . Notably, even in cases where the beyond-standard neutrino oscillation hypotheses scenarios are statistically indistinguishable, the measured value can exhibit significant deviations from its true value.

## I. INTRODUCTION

Neutrino flavor conversion is a well-established phenomenon, supported by extensive experimental evidence spanning nearly three decades [1–9]. The data indicate that neutrino flavor oscillation arises from the interference between different neutrino mass eigenstates, a process made possible because the mass eigenstates do not align with the flavor eigenstates [6–9]. However, the fact that neutrino oscillation is induced by non-zero and non-equal neutrino masses does not preclude the coexistence of subleading non-standard effects that may be beyond our current experimental sensitivity.

Alternative hypotheses that could play a subleading role in the neutrino oscillation mechanism or modify it include the violation of the equivalence principle by neutrinos [10, 11], non-standard interactions of neutrinos with matter [12, 13], neutrino decay [14, 15], and quantum decoherence [16, 17], among others [18–20]. Historically, some of these theoretical hypotheses were competitive solutions to either the solar neutrino problem [21, 22] or the atmospheric neutrino anomaly [23–25].

Upcoming neutrino long-baseline experiments will not only have enhanced sensitivities for measuring the CP violation phase and solving the neutrino mass hierarchy but also for exploring a new parameter range where these beyond-standard neutrino oscillation (BSO) phenomena may occur [26–28]. Many of these BSO phenomena have been individually studied within these under-development neutrino long-baseline experiments [29–38]. However, if we consider the existence of any BSO phenomena, an interesting question arises that needs further exploration: Shall we be able to distinguish a given BSO mechanism, present in nature, from other exotic phenomena or from the standard neutrino oscillations framework (SO)? Furthermore, how much would the measurement of the CP violation phase, the main objective of these experiments, be distorted if their ability to distinguish among BSO scenarios is not strong enough?

Our aim in this paper is to answer both questions in the context of the DUNE experiment [27, 28]. This will be achieved by performing a systematic statistical comparison between these BSO

\* [anthony.calatayud@pucp.edu.pe](mailto:anthony.calatayud@pucp.edu.pe)

† [alicia.perezg@pucp.edu.pe](mailto:alicia.perezg@pucp.edu.pe)

‡ [agago@pucp.edu.pe](mailto:agago@pucp.edu.pe)

scenarios and the SO one. Our goal is to provide a chart containing information about the statistical separation results from these comparisons and to highlight cases where a sizable discrepancy between the real and the measured  $\delta_{CP}$  phase occurs. For that purpose, we will test the following BSO scenarios: Violation of the Equivalence Principle, Non-Standard Interactions, Neutrino Decay, and Quantum Decoherence.

This paper is divided as follows: after the introduction, we discuss the theoretical formalism. Next, we present the analysis and simulation details, followed by the results section, and finalize with our conclusions.

## II. THEORETICAL FORMALISM

### A. Neutrino Oscillation Framework

The neutrino Hamiltonian in the flavor basis is given by:

$$H_{\text{osc}}^{fv} = \frac{1}{2E_\nu} \left( \mathbf{U} \Delta \mathbf{M}^2 \mathbf{U}^\dagger + \mathbf{A} \right), \quad (1)$$

where  $E_\nu$  represents the neutrino energy,  $\mathbf{U}$  is the Pontecorvo-Maki-Nakagawa-Sakata (PMNS) mixing matrix,  $\Delta \mathbf{M}^2$  is a diagonal mass matrix defined as  $\text{Diag}(0, \Delta m_{21}^2, \Delta m_{31}^2)$ , with  $\Delta m_{ij}^2 = m_i^2 - m_j^2$ . The diagonal matrix  $\mathbf{A}$  is given by  $\text{Diag}(A_{CC}, 0, 0)$ , encompassing the matter potential  $A_{CC} = 2\sqrt{2}G_F n_e E_\nu$ , where  $G_F$  and  $n_e$  denote the Fermi constant and the electron number density, respectively. The Hamiltonian above is the Standard Neutrino Oscillation framework in matter; any additional contributions beyond this scheme fall into the Beyond Standard Neutrino Oscillation category.

### B. Beyond Standard Neutrino Oscillation scenarios (BSO)

As mentioned in the introduction, the four theoretical hypotheses of BSO that we will be working on are the Violation of the Equivalence Principle, Non-Standard Interactions, Neutrino Decay, and Quantum Decoherence. For Non-Standard Interactions (NSI), we will explore two cases: one corresponds to the electron-muon conversion channel ( $\text{NSI}_{e\mu}$ ) and another corresponds to the electron-tau conversion channel ( $\text{NSI}_{e\tau}$ ). Neutrino Decay is subdivided into two sub-cases: Invisible Decay (ID) and Visible Decay (VD) (i.e., Full Decay).

The approach for incorporating the effects of the first two BSO hypotheses, Violation of the Equivalence Principle (VEP) and NSI, into the neutrino oscillation framework is the same. This entails adding a new term to the standard oscillation Hamiltonian, resulting in the following total Hamiltonian ( $H_{\text{osc}}^{\text{tot}}$ ):

$$H_{\text{osc}}^{\text{tot}} = H_{\text{osc}}^{fv} + H_{\text{BSO}}, \quad (2)$$

where  $H_{\text{BSO}}$  represents either the VEP contribution or the contribution from NSI. The procedure is quite similar for ID, but with the difference that the term added to  $H_{\text{osc}}^{fv}$  is anti-Hermitian. VD considers this, but due to the decay into active neutrinos, other details make calculating the oscillation probability cumbersome, as we will see later. Obtaining the neutrino oscillation probabilities including Quantum Decoherence effects differs from the preceding cases, requiring an open quantum system approach.

### 1. Violation of Equivalence Principle (VEP)

The Equivalence Principle posits that the gravitational acceleration experienced by an object is independent of its mass, and prompted Einstein to develop the General Theory of Relativity, which establishes the connection between the gravitational field and the curvature of space-time. The Violation of the Equivalence Principle (VEP) can be achieved through the breaking of the universality of Newton's gravitational constant,  $G_N$ , being redefined as  $G'_N = \gamma_i G_N$ , that implies a mass-dependent gravitational potential  $\Phi' = \gamma_i \Phi$ , where  $\gamma_i$  is a parameter that depends on the mass of the  $i$ th particle.

Under the assumption of the weak field approximation and making the appropriate substitutions and approximations into the space-time metric (see [29] for details), the following energy-momentum is obtained:

$$E_{\nu_i} \simeq p(1 + 2\gamma_i \Phi) + \frac{m_i^2}{2p}. \quad (3)$$

Considering that the momentum  $p \simeq E_\nu$ , with  $\Delta\gamma_{ij} = \gamma_i - \gamma_j$ , this leads to:

$$\Delta E_{ij} = \frac{\Delta m_{ij}^2}{2E_\nu} + 2E_\nu \Phi \Delta\gamma_{ij}. \quad (4)$$

The above equation implies that the mass and gravitational eigenstates are coincident bases. However, this might not be the case in a more generic scenario, as the mixing matrix connecting any of these eigenstates to the flavor basis may not be the same. Therefore, the translation of the above equations into a neutrino Hamiltonian in matter in its more generic form goes as follows:

$$H_{\text{osc}}^{\text{tot}} = H_{\text{osc}}^{fv} + 2E_\nu \Phi \mathbf{U}_{\mathbf{g}} \mathbf{\Delta}\gamma_{\mathbf{ij}} \mathbf{U}_{\mathbf{g}}^\dagger, \quad (5)$$

$\mathbf{U}_{\mathbf{g}}$  is the mixing matrix that connects the gravitational eigenstates with the flavor eigenstates, and  $\mathbf{\Delta}\gamma_{\mathbf{ij}} = \text{Diag}(0, \Delta\gamma_{21}, \Delta\gamma_{31})$ . For our analysis we assume  $\mathbf{U}_{\mathbf{g}} = \mathbf{U}$ ,  $\Delta\gamma_{21} > 0$ , and  $\Delta\gamma_{31} = 0$ , a particular case of Eq. (5).

### 2. Non-Standard Neutrino Interactions (NSI)

Since its introduction in [12, 13], the phenomenon that allows neutrino flavor transitions due to its interaction with matter, called neutrino non-standard interaction with matter (NSI), has been extensively studied [39–41]. There are several theories beyond the standard model of physics in which NSI processes are naturally derived (see [41] and references therein). NSI can occur during neutrino production, propagation, and detection, making it a very rich hypothesis from a phenomenological perspective [41, 42]. Given the goal of this work, we will only consider NSI during neutrino propagation in matter. With that purpose in mind, it is useful to provide the following effective neutral-current NSI Lagrangian:

$$\mathcal{L}_{eff}^{\text{NSI}} = -2\sqrt{2}\epsilon_{\alpha\beta}^{fP} G_F (\bar{\nu}_\alpha \gamma_\mu P_L \nu_\beta) (\bar{f} \gamma^\mu P f), \quad (6)$$

where  $f = e, u, d$ , and  $\alpha, \beta = e, \mu, \tau$ , while  $P$  stands for either  $P_L = \frac{1}{2}(1 - \gamma_5)$  or  $P_R = \frac{1}{2}(1 + \gamma_5)$ . Now, to write the total Hamiltonian for this case we need to define an effective  $\epsilon$  parameter,

$\epsilon_{\alpha\beta} = \sum_{f,P} \frac{n_f}{n_e} \epsilon_{\alpha\beta}^P$ , with  $n_f(n_e)$  are the  $f$ -type fermion number density. Thus, the total Hamiltonian is given by:

$$H_{\text{osc}}^{\text{tot}} = H_{\text{osc}}^{fv} + H_{\text{NSI}}, \quad (7)$$

where:

$$H_{\text{NSI}} = \sqrt{2}G_F n_e \begin{pmatrix} \epsilon_{ee} & \epsilon_{e\mu} & \epsilon_{e\tau} \\ \epsilon_{e\mu}^* & \epsilon_{\mu\mu} & \epsilon_{\mu\tau} \\ \epsilon_{e\tau}^* & \epsilon_{\mu\tau}^* & \epsilon_{\tau\tau} \end{pmatrix} \quad (8)$$

Here, the diagonal elements are real and are referred to as the lepton-universality breaking terms. Meanwhile, the non-diagonal elements represent the complex flavor transition terms and are defined as follows:

$$\epsilon_{\alpha\beta} = |\epsilon_{\alpha\beta}| e^{i\phi_{\alpha\beta}} \quad (9)$$

In our analysis, we will set all the diagonal elements to zero while turning on only a single non-diagonal parameter,  $\epsilon_{\alpha\beta}$ , and its complex conjugate, one at a time, with the rest of the parameters set to zero. Consequently, we will work with two different cases: one in which  $\epsilon_{e\mu}$  is activated (NSI $_{e\mu}$ ), and another with  $\epsilon_{e\tau}$  (NSI $_{e\tau}$ ), each being activated individually. The case of NSI $_{\mu\tau}$  will not be considered in our analysis since it is indistinguishable from the SO, further details can be seen in section III B.

### 3. Neutrino decay

Another way to modify standard neutrino oscillation is by allowing for the possibility that light neutrinos can decay. This hypothesis has been formulated based on the interaction of neutrinos with a massless scalar particle called the Majoron under two types of couplings, the scalar  $g_s$  and the pseudoscalar  $g_p$  (see [34] and references therein). These interactions are described by the Lagrangian below:

$$\mathcal{L}_{\text{int}} = \frac{(g_s)_{ij}}{2} \bar{\nu}_i \nu_j J + i \frac{(g_p)_{ij}}{2} \bar{\nu}_i \gamma_5 \nu_j J \quad (10)$$

Any of these terms can lead to neutrino decay such as  $\nu_j \rightarrow \nu_i + J$ , where  $J$  is the Majoron, and the  $\nu_j, \nu_i$  are the  $j, i$  neutrino-mass states. In our analysis, only the scalar coupling will be considered. Depending either on the ability to observe the final state neutrinos or whether they are active or not, neutrino decay can be classified in two ways:

- (a) **Invisible decay (ID)** In this scenario, the parent neutrino can decay either into a sterile neutrino or into an active neutrino that is not observable, due to its energy being below the experimental threshold. This leads to a modification in the total neutrino matter Hamiltonian, as described by the equation:

$$H_{\text{osc}}^{\text{tot}} = H_{\text{osc}}^{fv} - \frac{i}{2} \mathbf{U} \mathbf{T} \mathbf{U}^\dagger \quad (11)$$

For the present analysis, we will use  $\mathbf{T} = \text{Diag}(0, 0, \Gamma_3)$  for normal hierarchy, where  $\Gamma_3$  represents the decay rate of  $\nu_3 \rightarrow \nu_x$ . For inverted hierarchy, we consider  $\mathbf{T} = \text{Diag}(0, \Gamma_2, 0)$

for inverted hierarchy, where  $\Gamma_2$  represents the decay rate of  $\nu_2 \rightarrow \nu_x$ . The term  $-\frac{i}{2}\mathbf{U}\mathbf{\Gamma}\mathbf{U}^\dagger$  is anti-Hermitian, with  $\mathbf{U}$  being the PMNS matrix. Given that the  $H_{\text{osc}}^{\text{tot}}$ , due to the introduction of the anti-hermitian term, became an anti-hermitian one, this matrix will be diagonalized by a non-unitary matrix  $\tilde{\mathbf{U}}$  in the following way:

$$\tilde{\mathbf{U}}^{-1}H_{\text{osc}}^{\text{tot}}\tilde{\mathbf{U}} = \text{Diag}\left(\tilde{\lambda}_1, \tilde{\lambda}_2, \tilde{\lambda}_3\right) \quad (12)$$

with

$$\tilde{\lambda}_J = \frac{\tilde{m}_J^2}{2E_\nu} - i\frac{\tilde{\Gamma}_J}{2} \quad (13)$$

It is important to note that despite considering a single decay rate in the mass eigenstates basis, when we go to the effective matter eigenstates with the inclusion of matter effects, we can find non-zero values for all decay rates in this diagonalized basis. Therefore, the neutrino oscillation probability is given by [34]:

$$P_{\text{inv}}(\nu_\alpha \rightarrow \nu_\beta) = \left| \sum_J \tilde{U}_{\alpha J}^{-1} \exp\left[-i\frac{\tilde{m}_J^2 L}{2E_\alpha}\right] \exp\left[-\frac{\tilde{\alpha}_J L}{2E_\alpha}\right] \tilde{U}_{J\beta} \right|^2 \quad (14)$$

where  $J = 1, 2, 3$  and  $\tilde{\Gamma}_J = \frac{\tilde{\alpha}_J}{E_\alpha}$ , is the alternative parameter we will use to characterize neutrino decay from now on.

- (b) **Visible decay (Full decay)** The neutrino visible decay (VD) occurs when the decay products are (observable) active neutrinos with lower energies than their parent neutrinos. The full decay (FD) transition probability [34], which contains neutrino ID and VD contributions, goes as follows:

$$P_{\text{dec}}\left(\nu_\alpha^{(r)} \rightarrow \nu_\beta^{(s)}\right) = P_{\text{inv}}\left(\nu_\alpha^{(r)} \rightarrow \nu_\beta^{(s)}\right) \delta_{rs} \delta(E_\alpha - E_\beta) + P_{\text{vis}}(E_\alpha, E_\beta) \quad (15)$$

where the  $r = (+, -)$  and  $s = (+, -)$  are the helicities. The first term is the ID contribution (with the correspondence  $\tilde{U}_{\alpha j} \rightarrow \tilde{U}_{\alpha j}^{(r)}$  and  $\tilde{U}_{j\beta} \rightarrow \tilde{U}_{j\beta}^{(s)}$ ), which cannot change neutrino-helicities  $(r, s)$  during either the conversion or the survival. In addition, we must note that the neutrino mixing (in general) is related to the helicities as follows:  $\tilde{U}^{(-)} = \tilde{U}$  and  $\tilde{U}^{(+)} = \tilde{U}^*$ . Besides, in the ID the  $\nu_\alpha$  and  $\nu_\beta$  must have the same energy. To ensure the aforementioned conditions, the  $\delta_{rs}$  and  $\delta(E_\alpha - E_\beta)$  are added. The second term is the VD contribution, which, as expected, implies a degradation of the decaying neutrino energy  $E_\alpha$ , higher than the  $E_\beta$ . With minor modifications, here we are following the prescription for the  $P_{\text{vis}}$  in [34], which considers that the neutrino decays only once in its path:

$$\begin{aligned}
P_{\text{vis}}(E_\alpha, E_\beta) &= \int d\ell \left| \sum_J \left( \tilde{U}^{(r)} \right)_{\alpha J}^{-1} \exp \left[ -i \frac{\tilde{m}_J^2 \ell}{2E_\alpha} \right] \exp \left[ -\frac{\tilde{\alpha}_J \ell}{2E_\alpha} \right] \sum_{i=2}^3 \sum_{j=1}^{i-1} \tilde{C}_{Ji}^{(r)} \right. \\
&\quad \times \sqrt{\frac{d}{dE_\beta} \Gamma_{\nu_i^r \rightarrow \nu_j^s}(E_\alpha)} \sum_K \left( \tilde{C}^{(s)} \right)_{jK}^{-1} \exp \left[ -i \frac{\tilde{m}_K^2 (L - \ell)}{2E_\beta} \right] \\
&\quad \left. \times \exp \left[ -\frac{\tilde{\alpha}_K (L - \ell)}{2E_\beta} \right] \tilde{U}_{K\beta}^{(s)} \right|^2
\end{aligned} \tag{16}$$

with  $J, K = 1, 2, 3$ . It is important to note that  $\tilde{U}_{\alpha J}^{(r)}$ ,  $\tilde{m}_J^2$ ,  $\tilde{\alpha}_J$  and  $\tilde{C}_{Ji}^{(r)}$  are calculated using Eq. (12) with  $E_\nu = E_\alpha$ , while  $\tilde{U}_{K\beta}^{(s)}$ ,  $\tilde{m}_K^2$ ,  $\tilde{\alpha}_K$  and  $\tilde{C}_{Kj}^{(s)}$  are obtained for  $E_\nu = E_\beta$ . The reasoning behind the structure of  $P_{\text{vis}}$  is as follows: we initiate with a flavor (interaction) eigenstate  $\nu_\alpha$ , which is transformed into the matter eigenstate  $\tilde{\nu}_J$  before propagating a distance  $l$  prior to decay. In the decay process  $\nu_i^r \rightarrow \nu_j^s$ , we initially rotate from the  $\tilde{\nu}_J$  to the mass eigenstate  $\nu_i^r$  (where the decay is defined) using the operator  $\tilde{C}_{Ji}^{(r)}$ . After the decay, we revert the decay product, the mass eigenstate  $\nu_j^s$ , back to the matter eigenstate  $\tilde{\nu}_K$  with the inverse of the operator  $\tilde{C}_{Kj}^{(s)}$ . The  $\tilde{\nu}_K$  then propagates until it reaches the detector, where it is rotated into the flavor eigenstate  $\nu_\beta$ . The definition of the operator  $\tilde{C}$  is:

$$\tilde{C}_{Mn}^{(h)} = \sum_{\alpha=e,\mu,\tau} \tilde{U}_{\alpha M}^{(h)} (U)_{\alpha n}^{(h)*} \tag{17}$$

where  $U$  is a PMNS matrix element,  $h = (+, -)$  is the helicity, and  $M, n$  is a matter and mass eigenstate, respectively.

For FD, we will use  $\alpha_3^{vis} = \alpha_{\nu_3 \rightarrow \nu_1}$  for normal ordering (NO), referred to as FD1, and  $\alpha_2^{vis} = \alpha_{\nu_2 \rightarrow \nu_3}$  for inverted ordering (IO), referred to as FD2. We take a scalar coupling with  $m_1 = 0.05$  eV for both cases.

#### 4. Quantum decoherence (QD)

The neutrino system can be envisioned as an open quantum system subjected to the effects of its interaction with the environment [16, 17], which can be a manifestation of Planck-scale physics [43, 44]. These effects are typically revealed by introducing quantum decoherence (QD) parameters in the neutrino oscillation probabilities. However, it is also possible to have CPT violation effects [45, 46] or even be sensitive to the Majorana CP violation phase [47, 48], among others.

##### (a) The density matrix formalism

The way to describe the evolution of the neutrino system in a dissipative environment is by using the Lindblad master equation, which implies representing the neutrino system with the density matrix formalism. The Lindblad master equation is defined as follows [49]:

$$\frac{d\rho(t)}{dt} = -i [H, \rho(t)] + L[\rho(t)] \tag{18}$$

where  $H$  is the neutrino system Hamiltonian (that we will discuss later) and  $\rho(t)$  is the neutrino density matrix, while  $L[\rho(t)]$  is the term that encloses the dissipative effects. The  $L[\rho(t)]$  is given by [37]:

$$L[\rho(t)] = -\frac{1}{2} \sum_j \left\{ A_j^\dagger A_j \rho(t) + \rho(t) A_j^\dagger A_j \right\} + \sum_j A_j \rho(t) A_j^\dagger \quad (19)$$

The  $A_j$  are a set of operators with  $j = 1, 2, \dots, 8$ , for three-neutrino generations. These operators are hermitian to secure the increase of the Von Neumann entropy over time. Another step for solving the Eq. (18) is to write the operators  $\rho$ ,  $H$  and  $A_j$  as:

$$\rho = \frac{1}{2} \sum \rho_\mu \lambda_\mu, \quad H = \frac{1}{2} \sum h_\mu \lambda_\mu, \quad A_j = \frac{1}{2} \sum a_\mu^j \lambda_\mu \quad (20)$$

where  $\mu$  is running from 0 to 9,  $\lambda_0$  is the identity matrix and  $\lambda_k$  are the Gell-Mann matrices, which satisfy the relationship  $[\lambda_i, \lambda_j] = 2if_{ijk}\lambda_k$ , the  $f_{ijk}$  is the structure constant of  $SU(3)$ . The matrix  $L_{\mu\nu}(\equiv L[\rho(t)])$  is real and symmetric, and it can be expressed as  $L_{kj} = \frac{1}{2} \sum_{l,m,n} (\vec{a}_n \cdot \vec{a}_l) f_{knm} f_{mlj}$ , all of this due to the Hermiticity of the  $A_j$ , with the components  $L_{\mu 0} = L_{0\mu} = 0$ , because of the probability conservation. Additionally, the decoherence matrix  $\mathbf{L} \equiv L_{kj}$  must satisfy the Cauchy-Schwartz inequalities and the complete positivity condition, to ensure that the eigenvalues of  $\rho(t)$  are positive at any time. Taking all the above into consideration, Eq. (18) turns out to be:

$$\dot{\rho}_0 = 0, \quad \dot{\rho}_k = (H_{kl} + L_{kl}) \rho_l = M_{kl} \rho_l \quad (21)$$

with  $H_{kl} = \sum_j h_j f_{jlk}$ . Therefore, the solution of  $\rho(t)$  is:

$$\varrho(t) = e^{\mathbf{M}t} \varrho(0) \quad (22)$$

where  $\varrho$  is an eight columns vector and  $\mathbf{M} \equiv M_{kl}$ . The  $e^{\mathbf{M}t}$  is written as:

$$e^{\mathbf{M}t} = \mathbf{D} e^{\mathbf{M}_D t} \mathbf{D}^{-1} \equiv [e^{\mathbf{M}t}]_{il} = \sum_k D_{il} e^{\lambda_k t} D_{kl}^{-1} \quad (23)$$

with  $\mathbf{M}_D = \mathbf{Diag}(\lambda_1, \dots, \lambda_8)$ . Thus, the neutrino oscillation probability is given by:

$$P_{\nu_\alpha \rightarrow \nu_\beta} = \text{Tr} \left( \rho^\alpha(t) \rho^\beta \right) = \frac{1}{3} + \frac{1}{2} \sum_{i,j} \rho_i^\beta(0) [e^{\mathbf{M}t}]_{il} \rho_l^\alpha(0) = \frac{1}{3} + \frac{1}{2} (\varrho^\beta(0))^T \varrho^\alpha(t) \quad (24)$$

In this work the decoherence matrix is given by:  $\mathbf{L} = -\text{Diag}(0, 0, 0, \Gamma, \Gamma, \Gamma, \Gamma, 0)$  where the experimental bounds for  $\Gamma$  are well determined [50]. It is worth noting that QD disrupts the coherence pattern, resulting in damping factors as  $e^{-\Gamma L}$  multiplying the oscillatory terms contained in the neutrino flavor transition probability.

## (b) Neutrino Hamiltonian and rotation between quantum bases

We assume that decoherence effects are defined in the neutrino mass eigenstate basis, where the neutrino Hamiltonian is described as:

$$H_{\text{osc}}^{ms} = \mathbf{U}^\dagger H_{\text{osc}}^{fv} \mathbf{U} \quad (25)$$

To solve Eq. (21), we are following the recipe given in [49]. Thus, we must transform the aforementioned equation from the mass eigenstate basis to the matter eigenstate basis, where the Hamiltonian is diagonal and more manageable. For this purpose, we apply the unitary transformation:  $\mathbf{U}_T^\dagger O_v \mathbf{U}_T$ , where  $O_v$  can represent  $\rho$ ,  $H$ , or  $L[\rho(t)]$ , defined in the mass eigenstate basis. The matrix  $\mathbf{U}_T$  facilitates the rotation between matter eigenstates and mass eigenstates and is defined as  $\mathbf{U}_T = \mathbf{U}^\dagger \mathbf{U}_m$ , where the matrix  $\mathbf{U}_m$  is responsible for diagonalizing  $H_{\text{osc}}^{fv}$ .

## III. ANALYSIS AND SIMULATION DETAILS

### A. BSO quantification parameter $\xi$

To perform direct comparisons between the different BSO scenarios, we need to define a singular/equivalent parameter that quantifies the magnitude of the BSO effect relative to the standard one. We will denote this BSO strength parameter as  $\xi$ . For the cases of VEP and NSI, the identification of  $\xi$  would be done by considering the oscillatory term  $\frac{\Delta m^2}{4E} L \sim \mathcal{O}(1)$ . Therefore, as can be derived from Eq. (4), the BSO oscillatory term from VEP that perturbs its standard counterpart is  $E_\nu \Phi \Delta \gamma_{ij} L$ . Said perturbation is the  $\xi$  parameter for VEP. Similarly, for NSI, the corresponding  $\xi$  parameter is equal to  $2\sqrt{2} G_F n_e |\epsilon_{\alpha\beta}| L$ .

In the case of invisible neutrino decay, the size of its effect in distorting the SO formula is expressed through the magnitude of the exponential decay factor  $e^{-\frac{\alpha_3}{E_\nu} L}$  for NO or  $e^{-\frac{\alpha_2}{E_\nu} L}$  for IO. Thus, the corresponding BSO strength parameter for invisible decay is  $\xi = (\alpha_3/E_\nu) L$  for NO or  $\xi = (\alpha_2/E_\nu) L$  for IO. Meanwhile, in the case of visible decay or FD, the BSO strength parameter can be either  $\xi = (\alpha_3^{vis}/E_\nu) L$  for NO (FD1) or  $\xi = (\alpha_2^{vis}/E_\nu) L$  for IO (FD2). As we mentioned earlier, damping factor  $e^{-\Gamma L}$  characterizes the effects of QD in the neutrino oscillation probability, which is a factor that attenuates the oscillatory behavior of the latter. Therefore, as expected, for quantum decoherence, the  $\xi = \Gamma L$ . All the definitions of  $\xi$  for the different scenarios we study here are summarized in Table I, where for DUNE  $L = 1284.9$  km,  $\langle E_\nu \rangle = 2.6$  GeV and  $\rho = 2.848$  g/cm<sup>3</sup> [28]. The relationship between  $n_e$  and  $\rho$  is  $\rho = n_e/(Y_e N_A)$ , where  $N_A$  is the Avogadro constant and assuming the electron fraction  $Y_e = 0.5$ .

### B. $\xi$ parameter variation range and BSO experimental bounds

We will generate different sets of simulated true data for various BSO scenarios, each corresponding to a specific  $\xi$  parameter value within its defined range, with a maximum of 0.05. The correspondence between  $\xi = 0.05$  and each BSO scenario characteristic parameter used for generating its true simulated data is displayed in Table II.

In Table II are also displayed the experimental bounds for the different BSO scenarios. These bounds will act as upper limits, constraining the fitting range of the BSO scenarios when they play the role of the theoretical hypothesis. We have restricted the selected bounds to those extracted from man-made sources. Constraints on the NSI parameters  $\epsilon_{e\mu}$  and  $\epsilon_{e\tau}$  were obtained from [42].



BSO scenario	Strength parameter $\xi$
<b>VEP</b>	$\langle E_\nu \rangle \Phi \Delta \gamma_{21} L$
<b>NSI<math>_{e\mu}</math></b>	$2\sqrt{2} G_F n_e  \epsilon_{e\mu}  L$
<b>NSI<math>_{e\tau}</math></b>	$2\sqrt{2} G_F n_e  \epsilon_{e\tau}  L$
<b>ID (NO)</b>	$\frac{\alpha_3 L}{\langle E_\nu \rangle}$
<b>ID (IO)</b>	$\frac{\alpha_2 L}{\langle E_\nu \rangle}$
<b>FD (NO)</b>	$\frac{\alpha_3^{vis} L}{\langle E_\nu \rangle}$
<b>FD (IO)</b>	$\frac{\alpha_2^{vis} L}{\langle E_\nu \rangle}$
<b>QD</b>	$\Gamma L$

TABLE I: Definition of BSO strength parameter,  $\xi$ , for all scenarios considered.  $L$  and  $\langle E_\nu \rangle$  are the experiment baseline and average energy, respectively, in our case are the ones defined for the DUNE experiment.

BSO scenario	BSO parameter	Experimental upper bound	value at $\xi_{\max} = 0.05$
<b>VEP</b>	$\Phi \Delta \gamma_{21}$	$6.97 \times 10^{-23}$ [51]	$2.95 \times 10^{-24}$
<b>NSI<math>_{e\mu}</math></b>	$ \epsilon_{e\mu} $	$4.55 \times 10^{-2}$ [42]	$3.53 \times 10^{-2}$
<b>NSI<math>_{e\tau}</math></b>	$ \epsilon_{e\tau} $	$1.67 \times 10^{-1}$ [42]	$3.53 \times 10^{-2}$
<b>ID (NO)</b>	$\alpha_3$	$2.40 \times 10^{-4} \text{ eV}^2$ [52]	$2.00 \times 10^{-5} \text{ eV}^2$
<b>ID (IO)</b>	$\alpha_2$	$2.40 \times 10^{-4} \text{ eV}^2$ [52]	$2.00 \times 10^{-5} \text{ eV}^2$
<b>FD (NO)</b>	$\alpha_3^{vis}$	$7.80 \times 10^{-5} \text{ eV}^2$ [53]	$2.00 \times 10^{-5} \text{ eV}^2$
<b>FD (IO)</b>	$\alpha_2^{vis}$	$7.80 \times 10^{-5} \text{ eV}^2$ [53]	$2.00 \times 10^{-5} \text{ eV}^2$
<b>QD</b>	$\Gamma$	$4.80 \times 10^{-23} \text{ GeV}$ [50]	$7.68 \times 10^{-24} \text{ GeV}$

TABLE II: Experimental upper bounds for each BSO characteristic parameter and its value attained for the maximum  $\xi_{\max} = 0.05$ . The experimental bounds for VEP and NSI, are build from [51] and [42], the details are given in the text.

To maintain a conservative yet not overly restrictive approach, we consider the average of the strongest bounds given in Table 5 in [42]. This average includes the absolute value of the smallest limit from both the 90% and 99% confidence level intervals, as calculated in the analysis that incorporates NSI in electron scattering and CE $\nu$ NS (See [42] and references therein).

On the other hand, and as we said earlier, we will not take NSI $_{\mu\tau}$  as BSO true scenario, since this will not yield meaningful results in terms of distinguishing it from other BSO hypotheses (which serve as theoretical hypotheses) or showing noticeable distortions in the measurement of the CP violation phase relative to its true value, even for  $|\epsilon_{\mu\tau}| \sim \mathcal{O}(10^{-2})$ .

The experimental constraint for the VEP parameter, i.e., for  $\Phi \Delta \gamma_{21}$ , is translated from the Lorentz Invariance Violation bound for  $|a_{e\mu}|$  given at 90% C.L., and obtained in [51] using NO $\nu$ A [54, 55]. For this translation, we use Eq. (18) from [29], which defines the relation between  $\Phi \Delta \gamma_{21}$  and  $|a_{e\mu}|$  (equivalent to  $\tilde{\nu}_{e\mu}$  in [29]). It is worth mentioning that the resulting experimental constraint is one order of magnitude above the value corresponding to the maximum  $\xi$  used to simulate events with VEP (see Table II). In that sense, we can see that, in general, the BSO experimental bounds in Table II are above the maximum value that can be achieved for the true BSO parameters.

In Table III, we display the translation between the characteristic parameters of the different BSO scenarios and different values of the intensity parameter  $\xi$ , within our analysis range.

$\xi$	$\Phi\Delta\gamma_{21}[10^{-24}]$	$ \epsilon_{e\mu} ,  \epsilon_{e\tau} [10^{-2}]$	$\alpha_3, \alpha_2, \alpha_3^{vis}, \alpha_2^{vis}[10^{-5} \text{ eV}^2]$	$\Gamma[10^{-24} \text{ GeV}]$
0.005	0.30	0.35	0.20	0.77
0.010	0.60	0.70	0.40	1.54
0.020	1.18	1.41	0.80	3.07
0.030	1.77	2.12	1.20	4.61
0.040	2.36	2.83	1.60	6.14
0.050	2.95	3.53	2.00	7.68

TABLE III: Equivalency between the BSO characteristic parameters and different values of  $\xi$ , that will be part of our analysis range.

Standard parameter	Value for NO	Value for IO
$\theta_{12}[\circ]$	34.3	34.3
$\theta_{13}[\circ]$	8.53	8.58
$\theta_{23}[\circ]$	49.26	49.46
$\Delta m_{12}^2[10^{-5} \text{ eV}^2]$	7.50	7.50
$\Delta m_{13}^2[10^{-3} \text{ eV}^2]$	2.55	-2.45

TABLE IV: Neutrino standard oscillation parameters values (taken from [57]) fixed for the generation of all true BSO scenarios.

### C. Simulation details

The DUNE experiment [27, 28], whose main goals are to achieve precise measurements of  $\delta_{CP}$  and the neutrino mass ordering, is a long-baseline neutrino experiment currently under construction. DUNE consists of two detectors: the near detector and the far detector. The near detector will be located at  $\mathcal{O}(100\text{m})$  from the neutrino beam source, while the far detector, to be placed at 1284.9 km, will have 40 kt of fiducial-volume liquid Argon. These detectors will be impacted by a neutrino beam sent from Fermilab toward the Sanford Underground Research Laboratory (the far detector location), after traveling through the Earth with an average matter density of  $2.848 \text{ g/cm}^3$ . The neutrino beam will be produced from the collisions of 120 GeV protons with a beam power of 1.2 MW (i.e., 624 kt-MW-years of exposure), operating for 6.5 years in neutrino mode (FHC) and 6.5 years in antineutrino mode (RHC), the time periods that we will use in our simulation. Furthermore, for our analysis, we will take into account  $\nu_e, \bar{\nu}_e$  appearance and  $\nu_\mu, \bar{\nu}_\mu$  disappearance channels, following, for all purposes, the prescription given [37].

While the implementation of DUNE in GLoBES has been given by the collaboration and is widely used, BSO phenomena, such as VEP and NSI, have to be introduced into the package through already existing functions (registering new probability engines) or by changing the source code directly (modifying the hamiltonian defined in the package to be diagonalized).

More complex theoretical hypotheses such as ID, FD (in which the Hamiltonian is non-Hermitian), and QD (with the density matrix formalism) were computed by programming the probability functions externally and integrating them into the GLoBES event rates calculations. For QD, the SQuIDS [56] library was specifically used to calculate the probability quickly and efficiently.

The neutrino oscillation parameters given in in Table IV will be fixed along the generation of the BSO true simulated events, for all the different scenarios. For the simulation of the NSI true events, regardless of the case, we decided to fix the corresponding complex phase of the NSI parameters at  $-90^\circ$ , inspired by [58, 59].

### D. Statistical analysis

Our analysis strategy consists of generating a set of true simulated BSO data for different values of  $\xi$ , within a range between  $[0, 0.05]$ , and for a given true BSO scenario. Then, for each value of  $\xi$ , we perform a statistical comparison between the given BSO true scenario and each of the remaining BSO theoretical hypotheses, plus SO (the test scenario). Our  $\chi^2$  statistical test is defined for a fixed  $\xi$  as follows:

$$\chi_{\xi}^2(\vec{\kappa}) = \min_{\vec{\alpha}} \sum_{\text{ch}} \left\{ 2 \sum_i \left[ N_{\text{ch},i}^{\text{test}}(\vec{\kappa}, \vec{\alpha}) - N_{\text{ch},i}^{\text{true}}(\xi) + N_{\text{ch},i}^{\text{true}}(\xi) \ln \left( \frac{N_{\text{ch},i}^{\text{true}}(\xi)}{N_{\text{ch},i}^{\text{test}}(\vec{\kappa}, \vec{\alpha})} \right) \right] \right\} + \sum_j \left( \frac{\alpha_j}{\sigma_{\alpha_j}} \right)^2 + \left( \frac{\theta_{13}^{\text{true}} - \theta_{13}^{\text{test}}}{\sigma_{\theta_{13}}} \right)^2, \quad (26)$$

the first term is the summation of the appearance channels,  $\nu_e$  and  $\bar{\nu}_e$ , and the disappearance ones,  $\nu_{\mu}$  and  $\bar{\nu}_{\mu}$ , identified by the index  $\text{ch}$ ,  $i$  represents the number of each energy bin. As expected, the  $N_{\text{ch},i}^{\text{true}}(\xi)$  corresponds to the BSO true event rates for fixed  $\xi$  and a given hypothesis, while the  $N_{\text{ch},i}^{\text{test}}(\vec{\kappa}, \vec{\alpha})$  are the test events that could correspond to any of the other BSO or the SO hypotheses, depending on which scenario is under test. The  $N_{\text{ch},i}^{\text{test}}(\vec{\kappa}, \vec{\alpha})$  depends on  $\vec{\kappa} = (\vec{\zeta}, \delta_{CP}, \theta_{13})$  where, in most BSO scenarios,  $\vec{\zeta}$  is equal to the single characteristic parameter of the given BSO test hypothesis, with the exception of NSI, where  $\vec{\zeta} = (|\epsilon_{\alpha\beta}|, \phi_{\alpha\beta})$ . It is evident that for SO, working as a test hypothesis,  $\vec{\zeta} = 0$ .

The BSO parameter and  $\delta_{CP}$  are free, while we include a  $3\sigma$  prior for  $\theta_{13}$  for NO(IO), with  $\sigma_{\theta_{13}} \simeq 0.38^\circ (0.39^\circ)$  [57], this is the third term of the equation above. Therefore, for our statistical analysis, we consider that VEP, ID, FD, and QD test hypotheses have two degrees of freedom (d.o.f), NSI and SO have three and one d.o.f, respectively. To take into account the systematic uncertainties, the  $\vec{\alpha}$  nuisance parameters are included as normalization factors of the signal and background components of a given channel  $\text{ch}$ ; the standard deviations  $\sigma_{\alpha_j}$  are provided by the DUNE files for GLOBES [60]. The second term includes the penalty factors due to the systematic uncertainties  $\alpha_j$  with the standard deviation  $\sigma_{\alpha_j}$  and zero as expectation value.

Our  $\chi^2$  represents the minimization in  $\vec{\alpha}$  nuisance parameters for a fixed  $\vec{\kappa}$ . Therefore, the best-fit point is obtained by minimizing over  $\kappa$ :

$$\chi_{\xi,\text{min}}^2 = \min_{\vec{\kappa}} \{ \chi_{\xi}^2(\vec{\kappa}) \} = \chi_{\xi}^2(\vec{\zeta}^{\text{fit}}, \delta_{CP}^{\text{fit}}, \theta_{13}^{\text{fit}}), \quad (27)$$

where  $\vec{\zeta}^{\text{fit}}$ ,  $\delta_{CP}^{\text{fit}}$  and  $\theta_{13}^{\text{fit}}$  are the best fit parameters. Since our goal is to estimate the the statistical separation between BSO scenarios (true compared to test), and between BSO true scenario and SO as test, we will have to use the  $\Delta\chi^2$ :

$$\Delta\chi^2 = \chi_{\xi,\text{min}}^2 - \chi_{\xi,\text{min}(\text{true=test})}^2 \quad (28)$$

where the  $\chi_{\xi,\text{min}(\text{true=test})}^2$  is equal to zero and correspond to the case when the BSO true and the test scenario are the same.

### E. Plots description and guidelines

Our findings will be presented through two different types of plots:

- **$N_\sigma$  versus  $\xi$ :** This plot measures, for a given value of  $\xi$ , the  $N_\sigma$  separation between our true hypothesis and the fitted one, taking into consideration the number of d.o.f, where 1 d.o.f is used for SO, 3 d.o.f for the NSI scenarios and 2 d.o.f for the rest of BSO scenarios.
- **$\delta_{CP}$  versus  $\xi$ :** This plot shows the behavior of the  $\delta_{CP}$  fitted value as function of  $\xi$ . To asses the degree of discrepancy between the fit  $\delta_{CP}$  and the true  $\delta_{CP}$ , different levels of uncertainties of the latter are displayed. These uncertainties on the  $\delta_{CP}$  true value are determined for a given  $\xi$  value (i.e. according to its corresponding true BSO parameter).

At follows we present our guidelines for the plot presentation:

1. **Largest  $N_\sigma$  value:** We will display only plots  $N_\sigma$  versus  $\xi$  plots in which one or more of BSO or SO theoretical hypotheses tested reach an  $N_\sigma > 3\sigma$  separation relative to the corresponding BSO true hypothesis.
2. **The fitted  $\delta_{CP}$  reaches, at least, the  $3\sigma$  level of the true  $\delta_{CP}$  uncertainty:** We will display only plots  $\delta_{CP}$  versus  $\xi$  plots in which one or more of the fitted  $\delta_{CP}$  curves, obtained from testing a given BSO theoretical hypothesis as a true, approach, reach or surpass, the  $3\sigma$  level uncertainty of the true  $\delta_{CP}$ . As we already mentioned, the uncertainties have been determined per each  $\xi$  value.
3. **All fitted BSO parameters are within the experimental bounds:** All the BSO fitted parameters that construct the BSO curves displayed in the plots are below the experimental bounds. When a fitted BSO parameter exceeds the experimental bounds, it is not included in the curve. These discarded fitted points correspond to the discontinuities or blank regions in the BSO curves, which partially cover the  $\xi$  range.
4. **BSO trivial solutions:** To ensure that the effects of our fit scenarios are detectable by DUNE's sensitivity, we have established a lower fitting bound for each BSO parameter. This is a minimum value that they must reach to be considered a non-trivial solution, meaning it does not overlap with the SO scenario and significantly differs from it. This bound would correspond to take  $\xi = 0.005$ , one order of magnitude less than our strongest BSO true effect ( $\xi = 0.05$ ). The specific BSO parameters that result in a trivial solution are displayed in Table V.

BSO parameter	$\Phi\Delta\gamma_{21}$	$ \epsilon_{e\mu} ,  \epsilon_{e\tau} $	$\alpha_3, \alpha_2, \alpha_3^{vis}, \alpha_2^{vis}$ [eV <sup>2</sup> ]	$\Gamma$ [GeV]
<b>Lower fitting bound</b>	$2.95 \times 10^{-25}$	$3.53 \times 10^{-3}$	$2.00 \times 10^{-6}$	$7.68 \times 10^{-25}$

TABLE V: Lower fitting bounds for each BSO characteristic parameter. All the fitted parameters below these bounds is considered a BSO trivial solutions.

## IV. RESULTS

We will present our results separated by each BSO true scenario. As mentioned earlier, the  $|\epsilon_{\mu\tau}|$  scenario will not be included because there is no plot of either  $N_\sigma$  versus  $\xi$  or  $\delta_{CP}$  versus  $\xi$  for this scenario that fulfills our criteria 1 (for  $N_\sigma$ ) or 2 (the fitted  $\delta_{CP}$ ).

### A. VEP

In Fig. 1, we display the plots of  $N_\sigma$  vs  $\xi$  and  $\delta_{CP}$  vs  $\xi$  for both NO and IO, with  $\delta_{CP}^{true} = -90^\circ$ , since criteria 1 and 2 from our guidelines are satisfied. For NO, we see that FD is not plotted as a theoretical hypothetical solution because, within the whole range of  $\xi$ , it falls into the BSO trivial solution category. This means that the corresponding fitted parameters for FD are effectively zero (falling below the limits specified in Table. V), coinciding with the SO solution. For IO, we can observe that ID is the BSO trivial. On the other hand, a common characteristic of theoretical curves is that some of them may partially cover the entire range of  $\xi$ , showing discontinuities either at the beginning or at the end of the curve. For example, if they start at  $\xi > 0$ , it implies that the missing part of the curve corresponds to the BSO trivial solution category. Conversely, if the curves end at  $\xi < 0.05$  means that beyond this endpoint, the fitted parameters are excluded by experimental bounds. In the case where VEP, assuming NO, is taken as the true solution, the QD and ID ( $NSI_{e\mu}$ , and  $NSI_{e\tau}$ ) theoretical hypotheses exhibit beginning(ending) discontinuities. For IO, QD, and FD ( $NSI_{e\mu}$ ) correspond to beginning(ending) discontinuities cases. The  $N_\sigma = 5\sigma$  separation between the different theoretical hypotheses and the VEP simulated true data starts at  $\xi = 0.019, 0.021, 0.021$ , and  $0.027$  for SO, ID, QD, and  $NSI_{e\tau}$ , when NO is assumed. For IO the  $N_\sigma = 5\sigma$  begins at  $\xi = 0.016, 0.017$  and  $0.022$ , for SO, FD, and  $NSI_{e\tau}$ .

Regarding the discrepancy between the  $\delta_{CP}^{true} = -90^\circ$  and the fitted  $\delta_{CP}^{fit}$ , we observe that, for NO, a distortion of  $5(3)\sigma$  is achieved for  $NSI_{e\tau}$  when  $\delta_{CP}^{fit} = -125.81^\circ(-117.19^\circ)$  for  $\xi = 0.021(0.012)$ . It is expected to observe the highest distortion for  $NSI_{e\tau}$  at lower values of  $\xi$  since, in this scenario, the complex phase  $\phi_{e\tau}$  represents an additional d.o.f of variation. In the case of SO, ID, and QD a discrepancy around  $3\sigma$  is reached at  $\xi = 0.039, 0.042$  and  $0.047$  with  $\delta_{CP}^{fit} = -106.27^\circ, -105.65^\circ$  and  $-104.76^\circ$ , respectively. Similarly to the NO case, for IO,  $NSI_{e\tau}$  shows a  $5(3)\sigma$  discrepancy at  $\xi = 0.019(0.011)$  with  $\delta_{CP}^{fit} = -132.44^\circ(-121.18^\circ)$ . For the other scenarios, SO, QD, and FD, the distortions, at  $\xi = 0.05$ , are:  $3.3\sigma, 3.3\sigma$ , and  $3.1\sigma$ , with  $\delta_{CP}^{fit} = -105.95^\circ, -106.14^\circ$  and  $-104.69^\circ$ , respectively.

In Fig. 2 we show the plots corresponding to  $\delta_{CP}^{True} = 180^\circ$ . As we can observe, for the latter case and NO, there is no BSO trivial solution. However, for IO we have ID as BSO trivial solution. For NO (IO), the  $N_\sigma = 5\sigma$  separation is achieved when  $\xi = 0.018(0.015)$ . The highest deviation of the  $\delta_{CP}^{fit}$ , relative to the  $\delta_{CP}^{true} = 180^\circ$ , reaches, a maximum of approximately  $3\sigma$  for  $\xi = 0.029(0.050)$  with  $\delta_{CP}^{fit} = 168.64^\circ(170.92^\circ)$  for  $NSI_{e\tau}$ , and for both mass hierarchies. Additionally, for NO (IO),  $3\sigma(2.5\sigma)$  is reached for  $NSI_{e\mu}$  at  $\xi = 0.005(0.005)$  with  $\delta_{CP}^{fit} = 163.14^\circ(194.91^\circ)$ .

### B. NSI

In Fig. 3 we present our results when the true simulated data is generated for  $NSI_{e\mu}$ . For this case, only the plot  $\delta_{CP}^{fit}$  vs  $\xi$  passes the filter criteria, with SO, and  $NSI_{e\tau}$  being the only non-trivial solutions either NO or IO are assumed. Within this context, the IO case shows slightly higher discrepancies between  $\delta_{CP}^{fit}$  and  $\delta_{CP}^{true}$  compared to the NO case. On the other hand, the  $\delta_{CP}^{true} = -90^\circ$  exhibits stronger divergences than the case of  $\delta_{CP}^{true} = 180^\circ$ , following the same behavior as the case of VEP. The highest discrepancy is attained for IO and  $\delta_{CP}^{true} = -90^\circ$  reaching, approximately,  $5\sigma$  at  $\xi = 0.05$  with  $\delta_{CP}^{fit} = -137.82^\circ$ , for  $NSI_{e\tau}$  as theoretical hypothesis. The worst case combines NO and  $\delta_{CP}^{true} = 180^\circ$  attaining  $2.8\sigma$  at  $\xi = 0.05$  with  $\delta_{CP}^{fit} = 161.10^\circ$ , for SO.

The results for  $NSI_{e\tau}$  with  $\delta_{CP}^{true} = 180^\circ$ , when it is used for generating the true simulated data, are shown in Fig. 4. For this scenario, and NO, the SO, and  $NSI_{e\mu}$  are the non-trivial solutions. These solutions also remain trivial for the IO case with the addition of the ID solution. The maximal

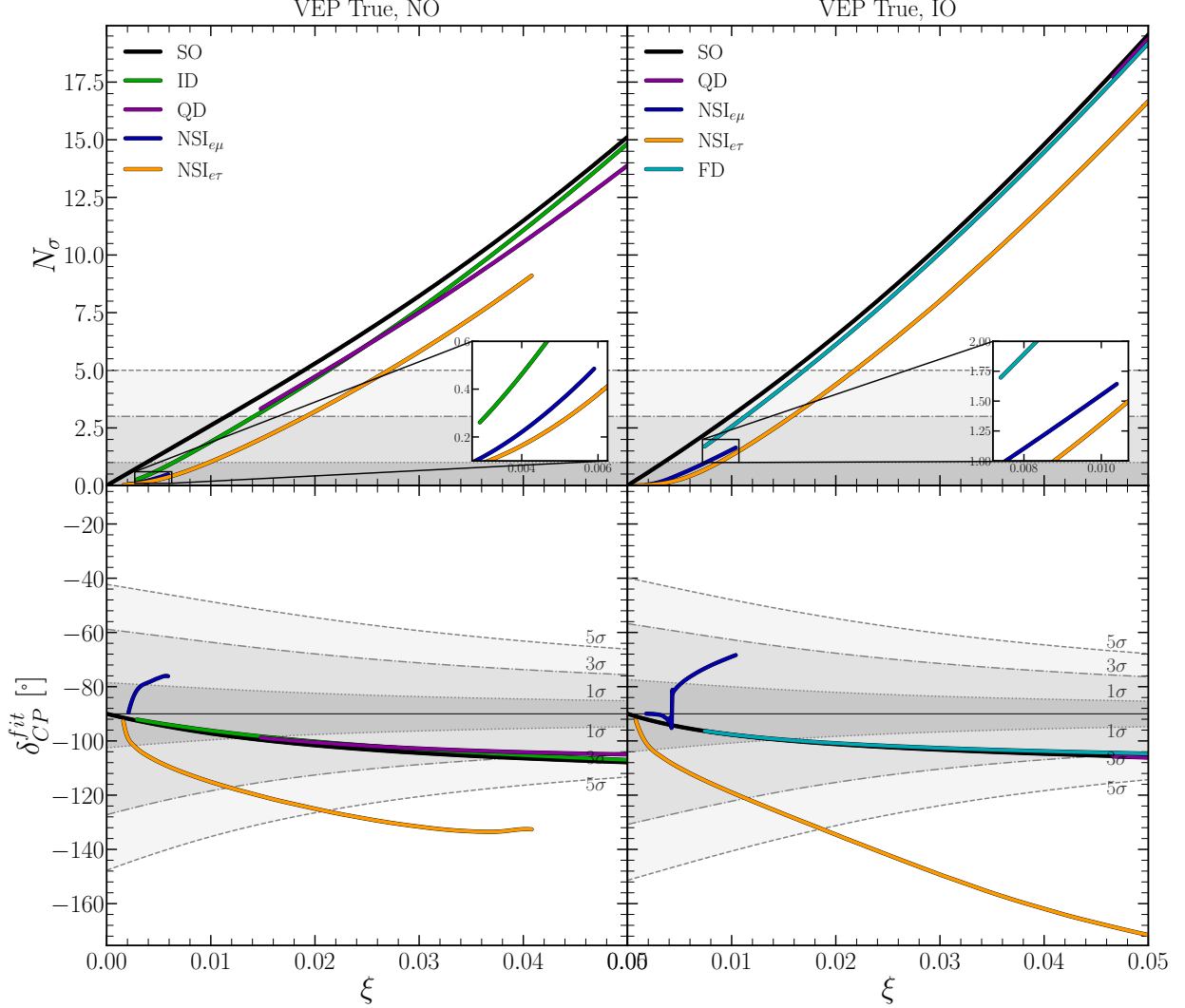


FIG. 1: VEP as a True Model. At the top is  $N_\sigma$  vs  $\xi$  and at the bottom is  $\delta_{CP}^{fit}$  vs  $\xi$ . All plots was made with  $\delta_{CP}^{true} = -90^\circ$ .

divergences between the  $\delta_{CP}^{true}$  and  $\delta_{CP}^{fit}$  are  $3.5\sigma$  and  $3.4\sigma$ , for ID and SO, respectively, and it is achieved at  $\xi = 0.05$ . These are obtained for IO with  $\delta_{CP}^{fit} = 206.46^\circ$  for ID and  $\delta_{CP}^{fit} = 205.75^\circ$  for ID and SO, respectively.

### C. ID

In Fig. 5 we display the plots of  $N_\sigma$  vs  $\xi$  for NO,  $\delta_{CP}^{true} = -90^\circ$  and  $\delta_{CP}^{true} = 180^\circ$ . In case of  $\delta_{CP}^{true} = -90^\circ$  QD and FD are trivial solutions, while for  $\delta_{CP}^{true} = 180^\circ$  VEP is added to the group of trivial solutions. For both values of  $\delta_{CP}^{true}$  the  $3\sigma$  significance is reached for  $\xi = 0.046$ .

The plots of  $\delta_{CP}^{fit}$  vs  $\xi$  are shown in Fig. 6. The trivial solutions for NO(IO) are VEP, QD, FD, and ID (VEP, QD, and ID). On the other hand, for NO (IO),  $2.4\sigma$  and  $2.7\sigma$  ( $3.8\sigma$ ) are(is) the highest separation of  $\delta_{CP}^{fit}$  achieved for NSI $_{e\mu}$  and NSI $_{e\tau}$  (NSI $_{e\tau}$ ) when  $\xi = 0.05$  and for  $\delta_{CP}^{fit} = 165.04^\circ$  and  $\delta_{CP}^{fit} = 163.02^\circ$  ( $\delta_{CP}^{fit} = 155.30^\circ$ ).

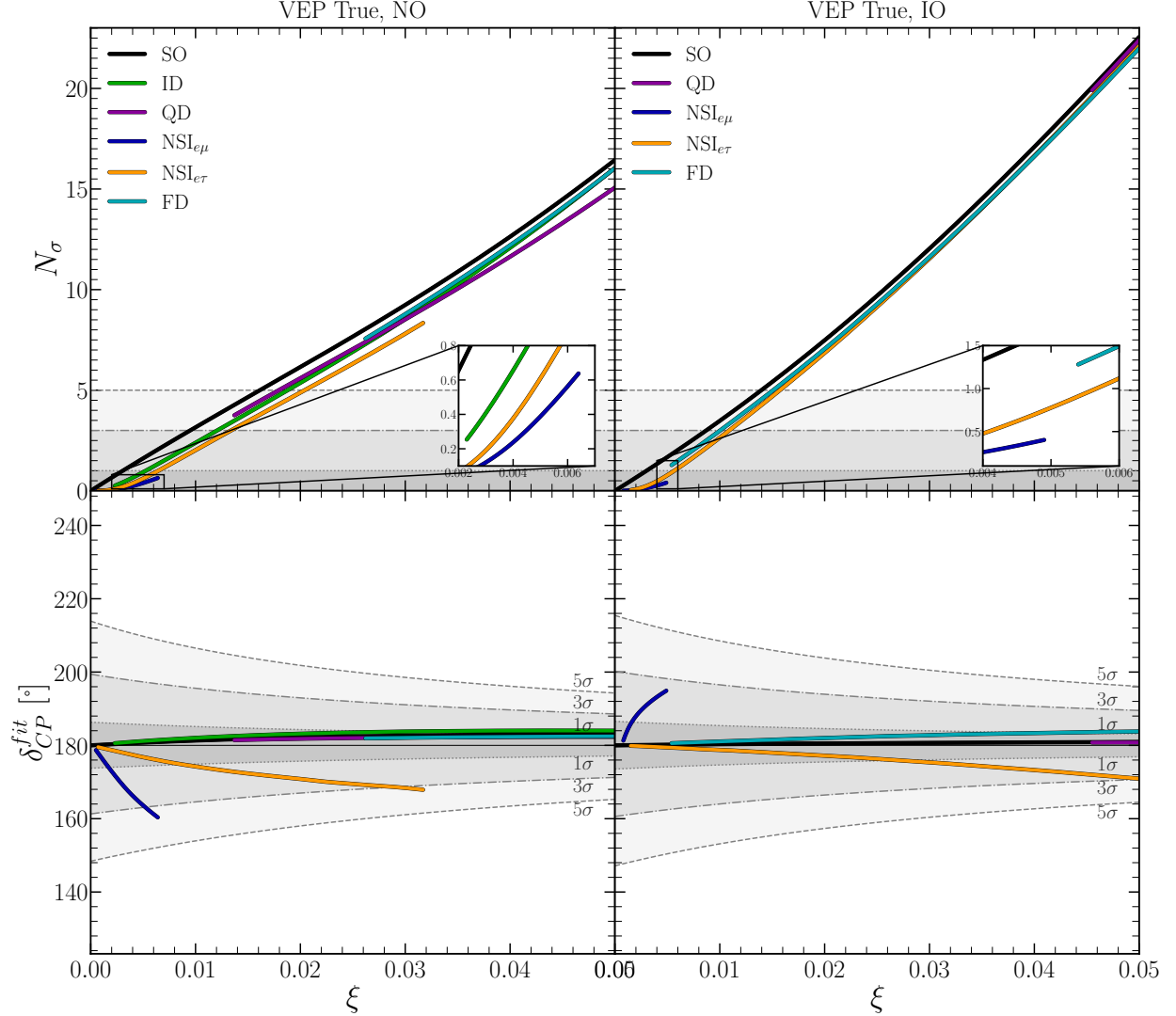


FIG. 2: VEP as a True Model. At the top is  $N_\sigma$  vs  $\xi$  and at the bottom is  $\delta_{CP}^{fit}$  vs  $\xi$ . All plots was made with  $\delta_{CP}^{true} = 180^\circ$ .

#### D. FD

We show the plots of  $N_\sigma$  vs  $\xi$  for NO,  $\delta_{CP}^{true} = -90^\circ$  and  $\delta_{CP}^{true} = 180^\circ$  in Fig. 7. The BSO trivial solutions for  $\delta_{CP}^{true} = -90^\circ$  ( $\delta_{CP}^{true} = 180^\circ$ ) are VEP, ID, and QD (QD). For  $\delta_{CP}^{true} = -90^\circ$  ( $\delta_{CP}^{true} = 180^\circ$ ), the  $5\sigma$  separation is attained for  $NSI_{e\tau}$  ( $NSI_{e\tau}$ ) at  $\xi = 0.020$  ( $\xi = 0.021$ ) while for SO it is reached at  $\xi = 0.017$  ( $\xi = 0.015$ ).

In Fig. 8 we present the plots of  $\delta_{CP}^{fit}$  vs  $\xi$  for NO with  $\delta_{CP}^{true} = -90^\circ$  and  $\delta_{CP}^{true} = 180^\circ$ , and for IO only the case  $\delta_{CP}^{true} = 180^\circ$  passes our filter criteria. We can observe that for NO and  $\delta_{CP}^{true} = -90^\circ$  the  $\xi = 0.042$ , for  $NSI_{e\tau}$ , is the minimal value where the  $5\sigma$  distortion is reached, with a value of  $\delta_{CP}^{fit} = -150.96^\circ$ . For  $\delta_{CP}^{true} = 180^\circ$  the  $3\sigma$  is the maximal divergence that can be obtained for  $NSI_{e\mu}$  at  $\xi = 0.009$ , being  $\delta_{CP}^{fit} = 199.94^\circ$ . The  $3\sigma$  distortion is the maximal that we can get for IO and  $\delta_{CP}^{true} = 180^\circ$ , with  $NSI_{e\tau}$  being the theoretical hypothesis with a fitted  $\delta_{CP}^{fit} = 160.56^\circ$  for  $\xi = 0.048$ .

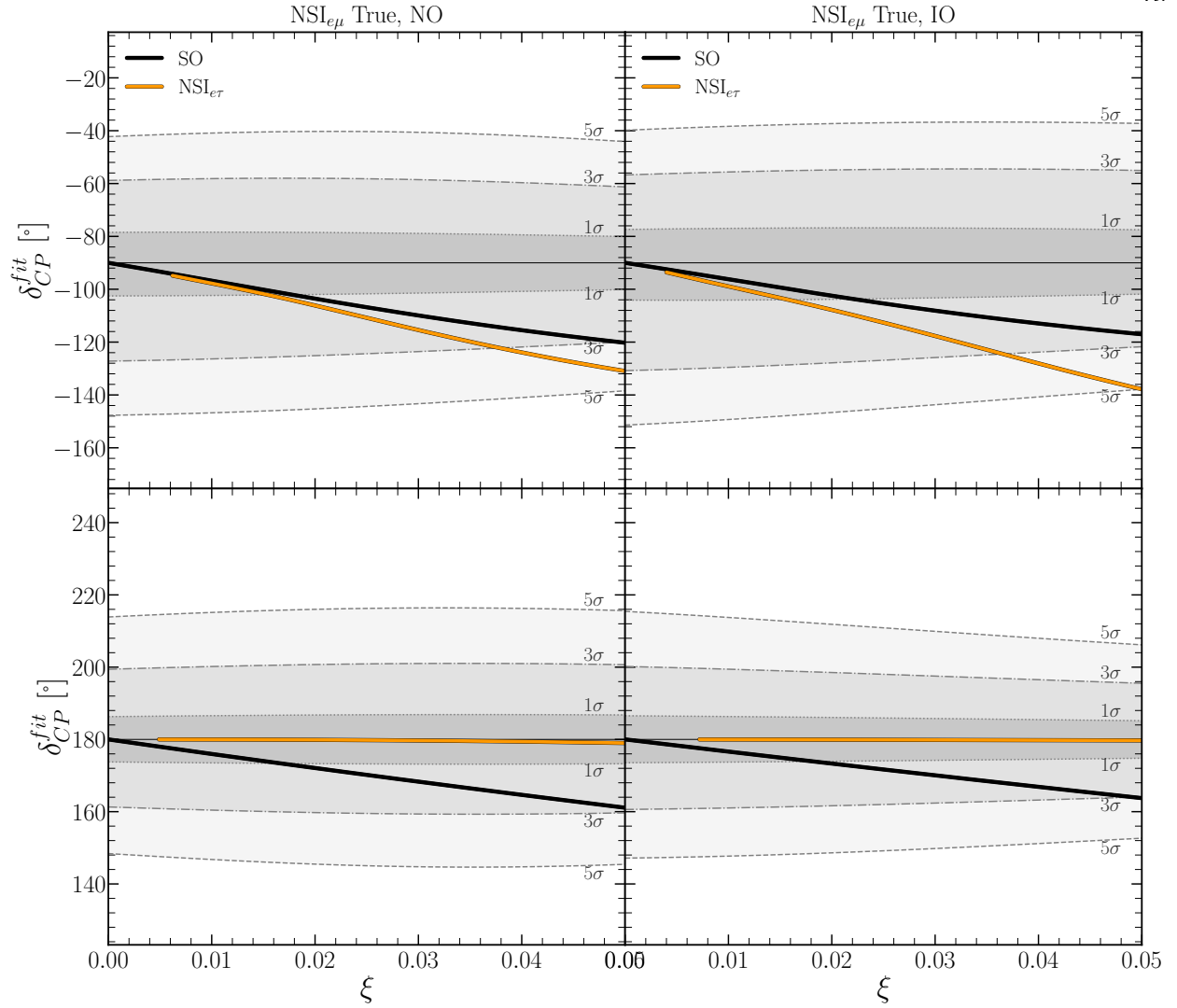


FIG. 3: NSI $_{e\mu}$  as a True Model. In the first row  $\delta_{CP}^{true} = -90^\circ$  and in the second row  $\delta_{CP}^{true} = 180^\circ$ .

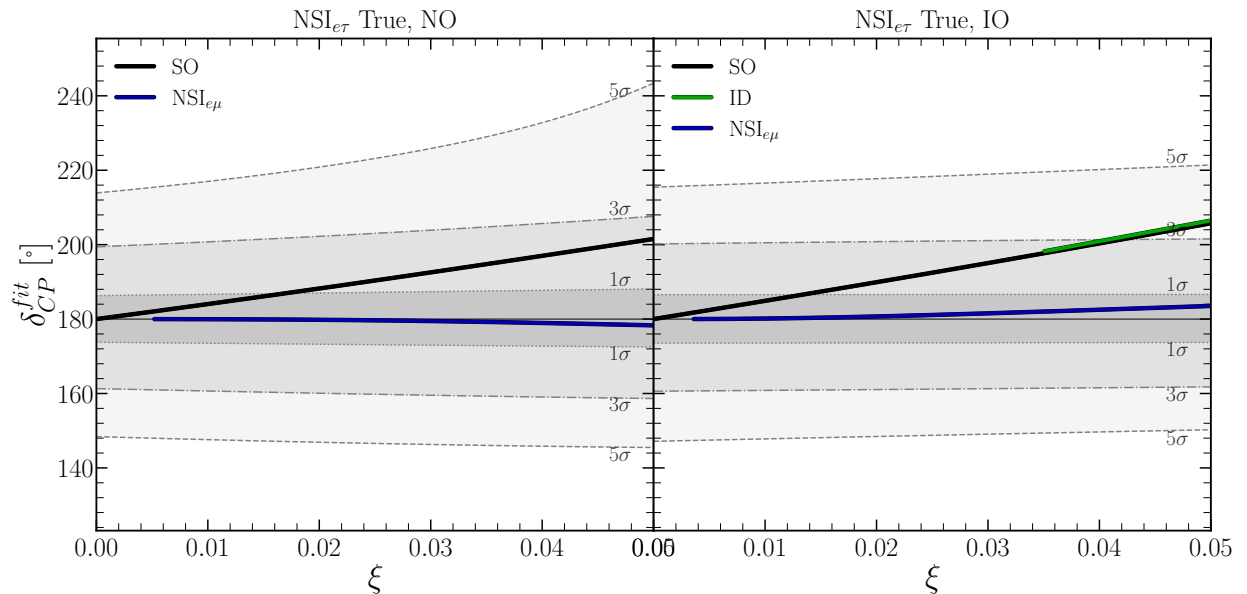


FIG. 4: NSI $_{e\tau}$  as a True Model. All plots was made with  $\delta_{CP}^{true} = 180^\circ$ .



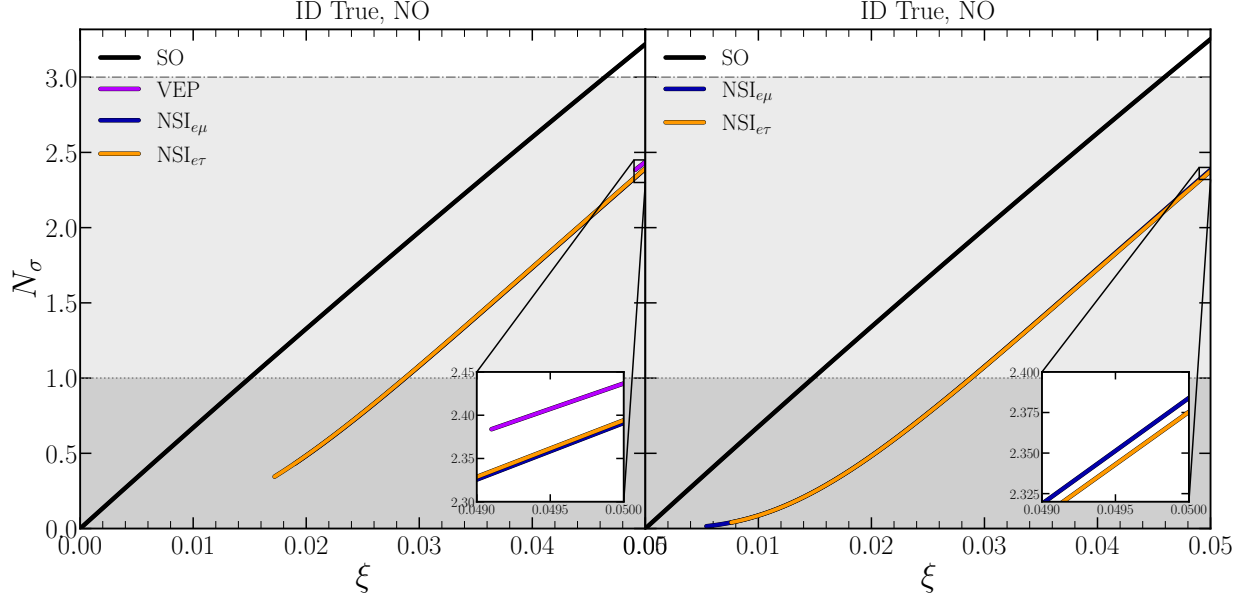


FIG. 5: ID as a True Model. Left plot has  $\delta_{CP}^{true} = -90^\circ$  and right plot has  $\delta_{CP}^{true} = 180^\circ$ .

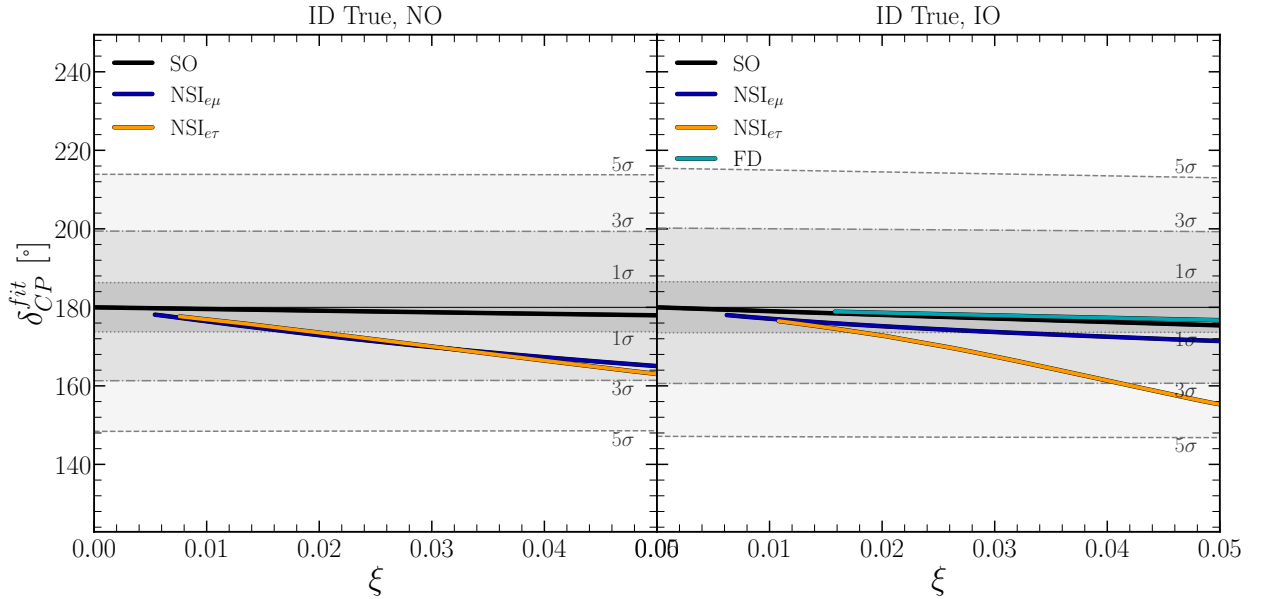


FIG. 6: ID as a True Model and  $\delta_{CP}^{true} = 180^\circ$ .

### E. QD

For QD only the plots  $N_\sigma$  vs  $\xi$  for NO,  $\delta_{CP}^{true} = -90^\circ$  and  $\delta_{CP}^{true} = 180^\circ$ , displayed in Fig. 9, survived our criteria. The BSO trivial solutions for NO (IO) are ID and FD for both values of  $\delta_{CP}^{true}$  (VEP for both  $\delta_{CP}^{true}$ , and  $NSI_{e\mu}$  for  $\delta_{CP}^{true} = 180^\circ$ ). For NO, and  $\delta_{CP}^{true} = -90^\circ$ , VEP and surpass the  $5\sigma$  separation when  $\xi = 0.032$ . For IO, the  $5\sigma$  separation is achieved at  $\xi = 0.033$  and  $0.032$  for ID, and  $NSI_{e\tau}$ , respectively. For  $\delta_{CP}^{true} = 180^\circ$  and NO (IO) the  $5\sigma$  separation is reached at  $\xi = 0.031$ , and  $0.031$  ( $\xi = 0.032$  and  $0.032$ ) for  $NSI_{e\mu}$ , and  $NSI_{e\tau}$  (ID, and  $NSI_{e\tau}$ ), respectively. Furthermore, for NO, and  $\delta_{CP}^{true} = 180^\circ$ , the VEP theoretical solution starts its appearance at  $\xi = 0.042$  achieving, at this value, a separation close to  $7.4\sigma$ .

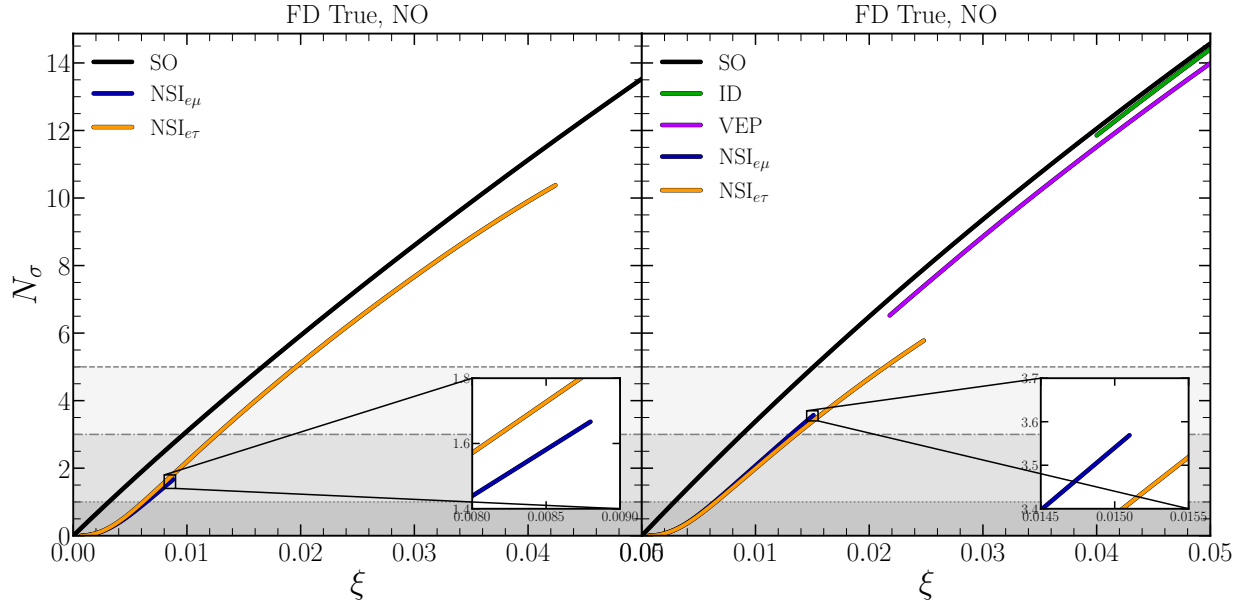


FIG. 7: FD as a True Model. Left plot has  $\delta_{CP}^{true} = -90^\circ$  and right plot has  $\delta_{CP}^{true} = 180^\circ$ .

## F. Findings overview

Below, we present a set of tables that will help us put into perspective the numerous results shown in the preceding section. These tables provide a panoramic and comparative overview, facilitating the drawing of general conclusions.

In each box, our tables pair a given true model (simulated data) with a fit model (theoretical hypothesis). All boxes in the tables are color-coded to highlight the quantity of interest related to the aforementioned pair analysis.

### 1. $N_\sigma$ summary

We have two types of tables. One type, presented in Table VI, is built using all the results from our  $N_\sigma$  analysis. The boxes of the tables, that correspond to specific true and fit model combinations, are color-coded to indicate the  $\xi$  value at which a given fit model shows a  $3\sigma$  discrepancy from the true model. If this value of  $\xi$  is below the upper limit of our range (0.05), it is clear that there is still room for achieving  $N_\sigma$  higher than  $3\sigma$ , that would correspond to higher values of  $\xi$ . As we have seen from our previous plots, the pair values of  $N_\sigma$  and  $\xi$  are connected by an almost linear relationship. The gray boxes represent cases where the statistical separation between the given true model and the fit model is below the  $3\sigma$  level.

A particular note: the numbers in some of the boxes indicate the values of  $N_\sigma$  for cases of initial discontinuities, where part of the curve is missing from the starting point to a specific point. For these special cases, the  $N_\sigma$  separation for a given box could start from values higher than  $3\sigma$ .

Regarding the results from Table VI, if QD is the true model, and we have IO and  $\delta_{CP}^{true} = -90^\circ$ , most of the theoretical hypotheses (fit models), except VEP, can be discriminated at  $3\sigma$  or more, depending on the value of  $\xi$  (the true parameter of QD). For instance, the SO, as a fit model, can be discriminated from QD if the true parameters of the latter correspond to  $\xi \gtrsim 0.016$  ( $\Gamma \gtrsim 2.46 \times 10^{-24}$  GeV), a low value in our scale of the QD parameter. On the other hand, when FD is the fit model, the true QD parameters correspond to  $\xi \gtrsim 0.034$  ( $\Gamma \gtrsim 5.22 \times 10^{-24}$  GeV). The rest of the fit models,  $\text{NSI}_{e\mu}$ , and  $\text{NSI}_{e\tau}$ , can be discriminated from QD starting at intermediate values such as

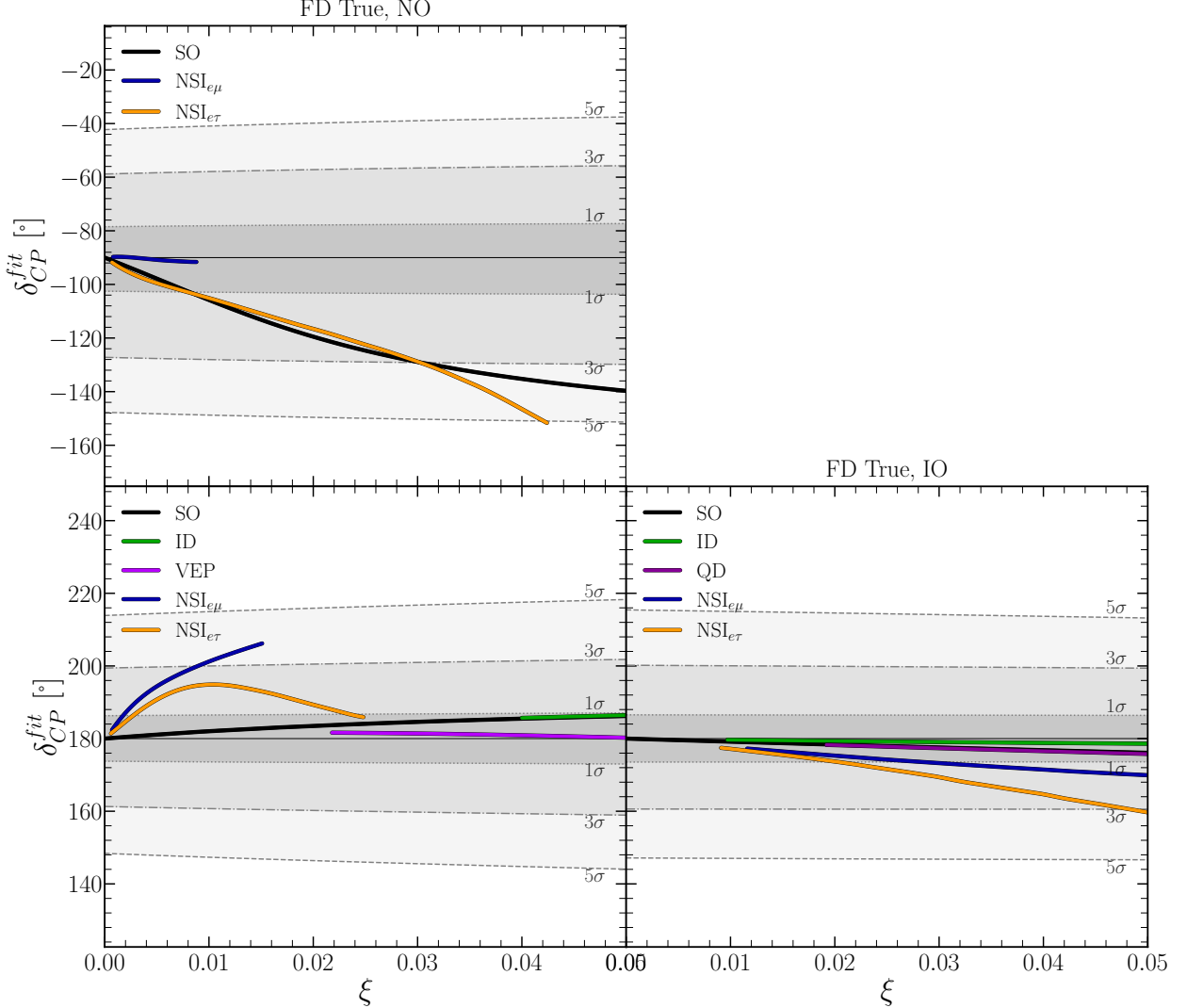


FIG. 8: FD as a True Model. In the first row  $\delta_{CP}^{true} = -90^\circ$  and in the second row  $\delta_{CP}^{true} = 180^\circ$ .

$\xi \gtrsim 0.021$  ( $\Gamma \gtrsim 3.23 \times 10^{-24}$  GeV).

The second true model exhibiting the highest discriminating power (from a theoretical hypothesis) is VEP, with NO and  $\delta_{CP}^{true} = 180^\circ$ , achieving a separation of  $3\sigma$  (or greater for the boxes with numbers) for SO, ID, QD, NSI $_{e\tau}$ , and FD, with values of  $\xi \gtrsim 0.009, 0.012, 0.014, 0.013$ , and  $0.026$  ( $\Phi\Delta\gamma_{21} \gtrsim 5.60 \times 10^{-25}, 7.13 \times 10^{-25}, 8.09 \times 10^{-25}, 7.90 \times 10^{-25}, 7.99 \times 10^{-25}$  and  $\Phi\Delta\gamma_{21} \gtrsim 1.55 \times 10^{-24}$ ), respectively. In general, for all the different combinations of mass hierarchy and  $\delta_{CP}^{true}$ , QD and VEP are the easiest true models to distinguish from the fit ones.

If FD is selected as the true model, assuming NO, it shows moderate discriminating power compared to QD and VEP. For FD with NO and  $\delta_{CP}^{true} = 180^\circ$ , the best capacity of distinction from other hypotheses is achieved, such as SO and NSI $_{e\tau}$  is a  $3\sigma$  separation or more for  $\xi \gtrsim 0.009$  ( $\alpha_3^{vis} \gtrsim 3.52 \times 10^{-6}$  eV $^2$ ) and  $\xi \gtrsim 0.014$  ( $\alpha_3^{vis} \gtrsim 5.42 \times 10^{-6}$  eV $^2$ ), respectively. For ID and VEP, the possible discrepancies start at  $11.9\sigma$  and  $6.5\sigma$ , for  $\xi \gtrsim 0.040$  ( $\alpha_3^{vis} \gtrsim 1.60 \times 10^{-5}$  eV $^2$ ) and  $\xi \gtrsim 0.022$  ( $\alpha_3^{vis} \gtrsim 8.70 \times 10^{-6}$  eV $^2$ ), respectively.

For FD with IO and both values of  $\delta_{CP}^{true}$ , and all cases of NSI for all combinations of mass hierarchies and both  $\delta_{CP}^{true}$ , the true cases are non-distinguishable at the  $3\sigma$  level (or more) for the given range we explore for  $\xi$ .

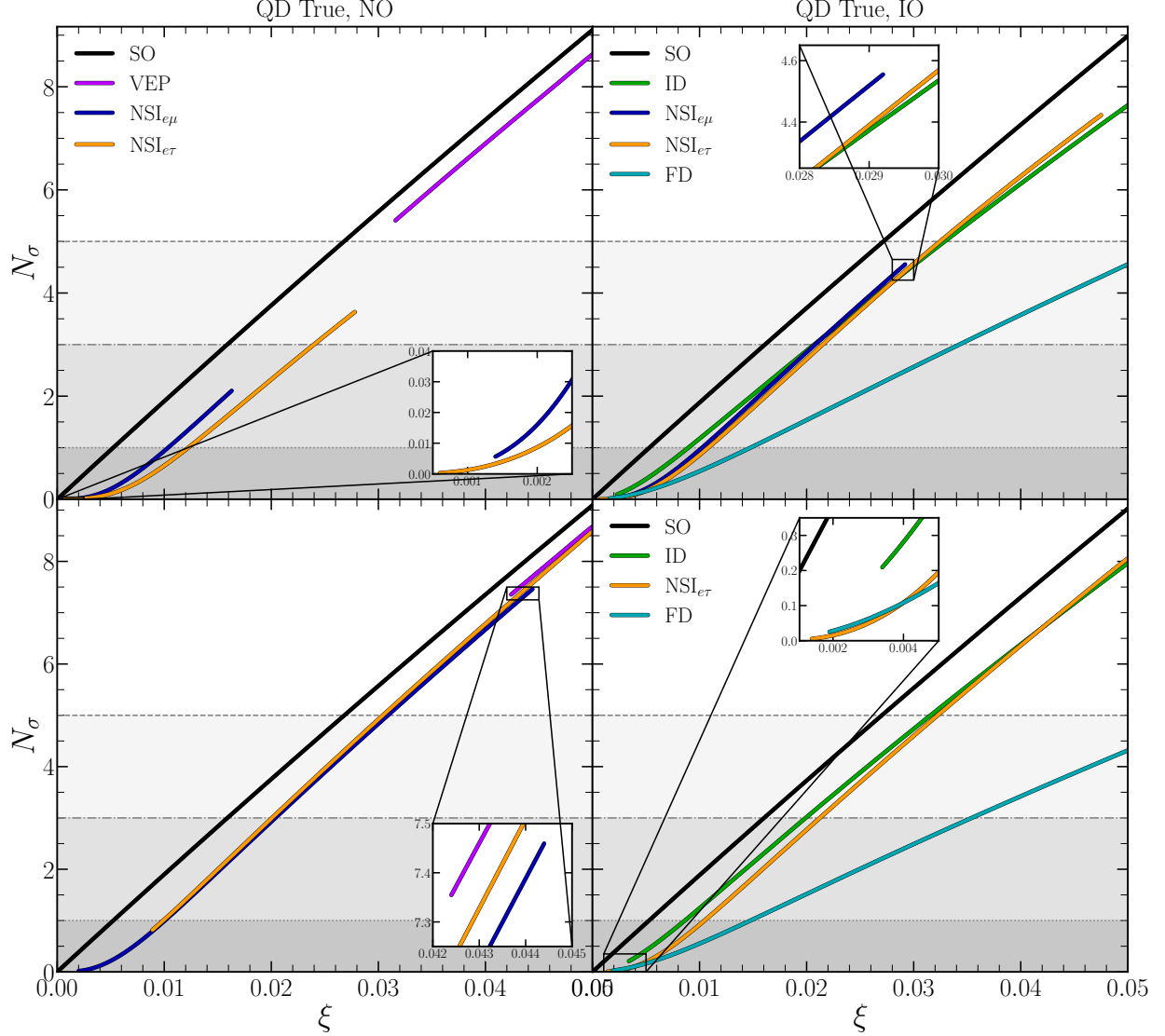


FIG. 9: QD as a True Model. In the first row  $\delta_{CP}^{true} = -90^\circ$  and in the second row  $\delta_{CP}^{true} = 180^\circ$ .

It should be noted that if the NO scheme is considered, we can discriminate SO from the QD, VEP, ID, and FD (true models).

## 2. $\delta_{CP}$ summary

In Table VII, the color code in the boxes (excluding the gray ones) indicates the value of  $\delta_{CP}^{fit}$  that deviates from the true one at which a given number of standard deviations ( $\sigma$ ) is attained. This quantity is not fixed for all the boxes of the different tables and can vary from  $2.4\sigma$  to  $3.1\sigma$ .

For instance, the  $2.4\sigma$  separation, the lower bound of the interval, occurs for VEP (true) and  $NSI_{e\mu}$  (fit), given  $\delta_{CP}^{true} = -90^\circ$  and NO, and for the pair  $NSI_{e\tau}$  (true) and SO (fit), given  $\delta_{CP}^{true} = 180^\circ$  and NO,. The higher extreme case of  $3.1\sigma$  separation occurs for the VEP(true) and QD(fit) pair with  $\delta_{CP}^{true} = -90^\circ$  and IO assumed. The grey boxes represent the pairs where the deviation of  $\delta_{CP}^{true}$  from  $\delta_{CP}^{fit}$  is below the lower bound of the aforementioned interval. The number inside the boxes denotes the  $N_\sigma$  for the given pair.

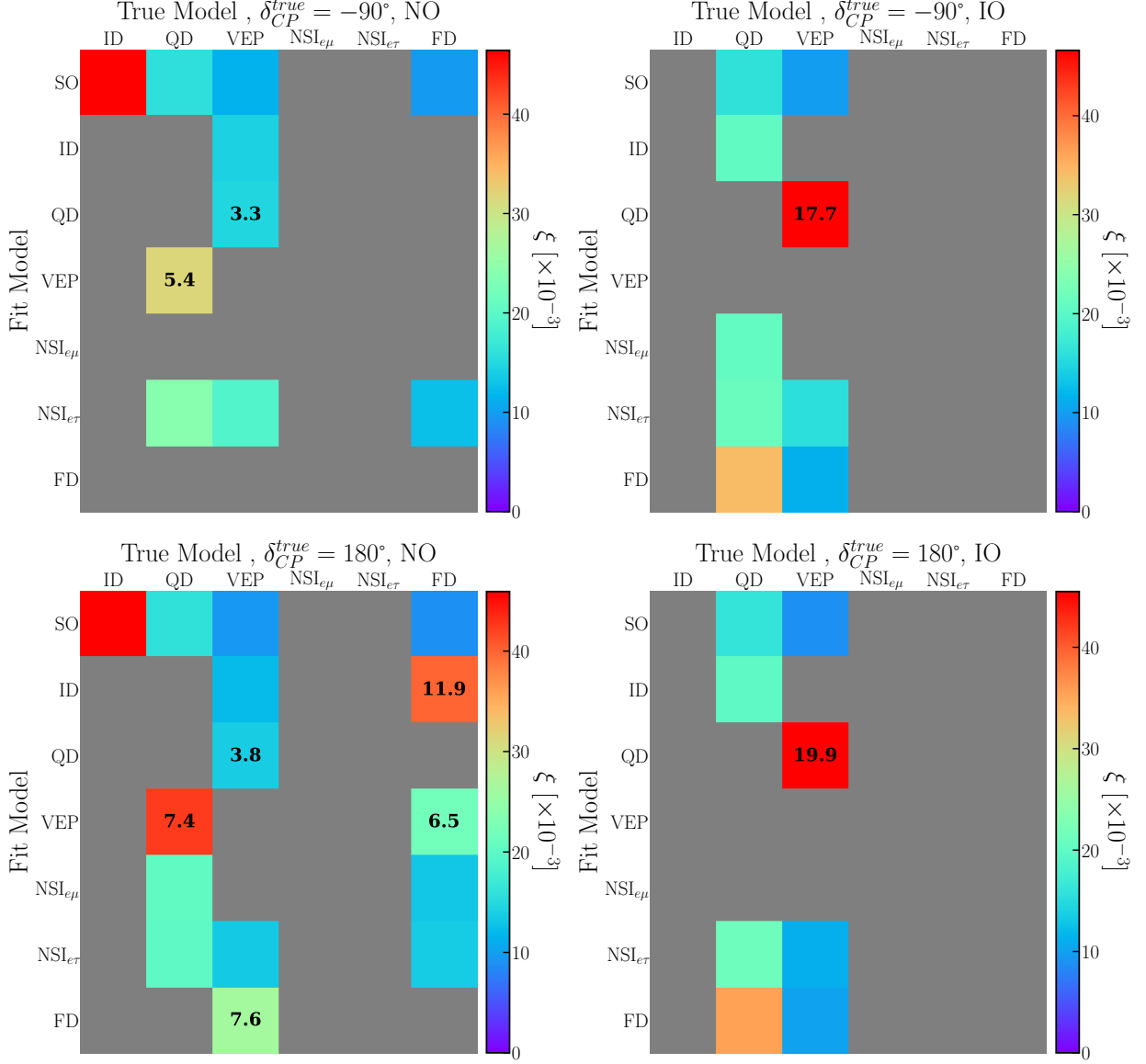


TABLE VI: Table of True Models vs Fit Models in which the value of  $\xi$  is shown for which  $N_\sigma = 3\sigma$  is obtained. The boxes displaying numbers indicate the cases where  $N_\sigma > 3\sigma$  and the number shown is the  $N_\sigma$  obtained.

Here, we can observe very challenging cases (from a statistical perspective) where a given pair (true and fit model) could have a very small  $N_\sigma$  separation but a sizable deviation between  $\delta_{CP}^{fit}$  and  $\delta_{CP}^{true}$ . The most extreme case is for the NSI<sub>eμ</sub>(true) and NSI<sub>eτ</sub>(fit) pair, for  $\delta_{CP}^{true} = -90^\circ$ , where  $N_\sigma = 0.3\sigma$ , while, contrastingly, the deviation between  $\delta_{CP}$ 's is  $3\sigma$  with  $\delta_{CP}^{fit} = -122.23^\circ$  and  $-124.50^\circ$ , for NO and IO, respectively. The second remarkable case with a similar tendency is for the VEP(true) and NSI<sub>eμ</sub>(fit) pair, considering  $\delta_{CP}^{true} = 180^\circ$  and NO. Here  $N_\sigma = 0.4\sigma$  while the separation between  $\delta_{CP}^{fit}$  and  $\delta_{CP}^{true}$  is  $3\sigma$ . For the same pair and IO, we also obtained  $N_\sigma = 0.4\sigma$ , being  $2.5\sigma$  the separation between  $\delta_{CP}$ .

There are several other cases where a similar contrast is maintained, with a low value of  $N_\sigma < 2\sigma$  and a  $\sigma$  separation between  $\delta_{CP}$ 's above  $2.4\sigma$ . The common factor in these cases is that NSI is involved either as the true model, the fit model, or both. The latter can be rather expected since the NSI hypotheses have an additional degree of freedom (the CP phase) relative to the other BSO

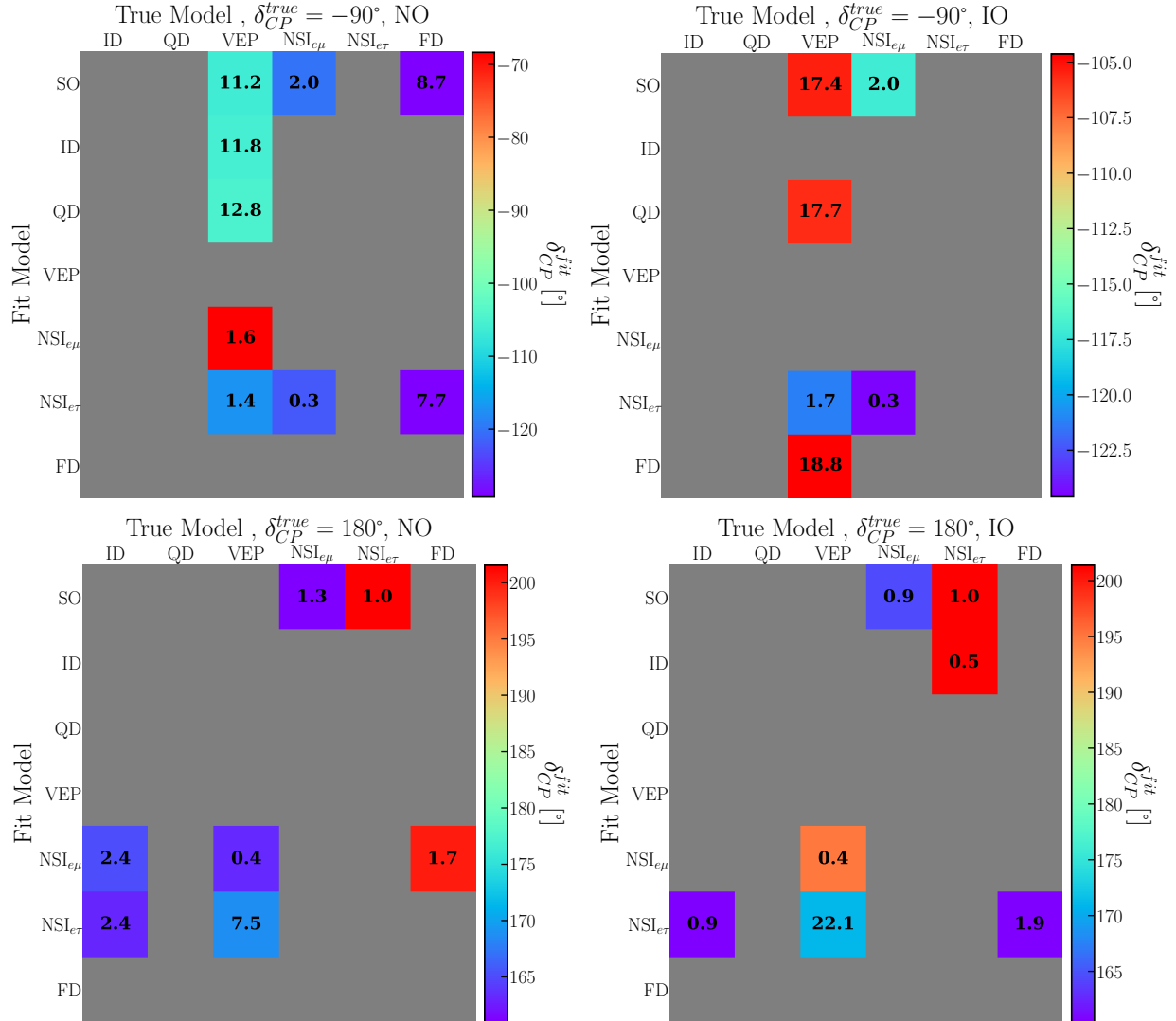


TABLE VII: Table of True Models vs Fit Models in which the values of  $\delta_{CP}^{fit}$  are when the deviation respect to  $\delta_{CP}^{true}$  is around  $2.4\sigma$ . The boxes displaying numbers indicate the respective  $N_\sigma$ .

hypotheses.

On the other hand, there are cases where the true and fit model pairs are highly distinguishable statistically (high  $N_\sigma$ ). In these types of cases, it would be expected that a relevant deviation between  $\delta_{CP}^{fit}$  and  $\delta_{CP}^{true}$  (above  $2.4\sigma$ ) would be disregarded as a controversial result.

## V. CONCLUSIONS

From the six BSO hypotheses used as DUNE true (simulated) data, we found that QD and VEP are the most distinguishable from the other BSO hypotheses and SO. For instance, QD can be discriminated, at the  $3\sigma$  level and higher, from SO, and NSI<sub>eτ</sub>, regardless of the neutrino mass hierarchy and the value of  $\delta_{CP}^{true}$ . QD can also be differentiated from ID and FD (VEP), for IO (NO) and for both values of  $\delta_{CP}^{true}$ . The maximum discrimination sensitivity for QD is achieved when the fit model is SO, and for  $\delta_{CP}^{true} = -90^\circ$  and NO, with the range of decoherence parameter values

that allow us to discriminate from  $3\sigma$  and above starting from  $\Gamma \gtrsim 2.44 \times 10^{-24}$  GeV. Besides, SO, the second best QD sensitivity, when the fit model is a BSO hypothesis, corresponds to ID with  $\Gamma \gtrsim 3.06 \times 10^{-24}$  GeV, and for  $\delta_{CP}^{true} = 180^\circ$  and IO.

The discriminating power of VEP, when used as simulated true data, is almost equal to QD. Similar to the latter, VEP can be differentiated from SO, QD, and  $\text{NSI}_{e\tau}$  no matter the hierarchy scheme or the values of  $\delta_{CP}^{true}$  used. It can also be distinguished from FD for almost all cases, while the distinction between VEP and ID could happen for NO and for both  $\delta_{CP}^{true}$  values. When VEP is compared against SO, the maximum range of sensitivity is attained with the  $\Phi\Delta\gamma_{21} \gtrsim 5.84 \times 10^{-25}$ . Now, when the fit model is a BSO hypothesis, the best sensitivity is for FD, with the range of VEP parameters able to make the distinction (at the  $3\sigma$  level and above) given by  $\Phi\Delta\gamma_{21} \gtrsim 5.93 \times 10^{-25}$ . On the other hand, if any of the three NSI hypotheses is present in nature, DUNE will be unable to unravel any of it, unless above or equal to the  $3\sigma$  level, from the other BSO alternatives studied here.

Our analysis, which measures the distortion between the fitted  $\delta_{CP}$  and its true value within the context of model comparisons, indicates that it is possible to have a significant separation between the fitted and true  $\delta_{CP}$ . At the same time, the models under comparison can be very close, i.e., separated by less than  $2\sigma$ . The common factor in the aforementioned cases is the involvement of the NSI hypotheses, either in comparisons among them or with other models. The situation described before is somewhat expected since our NSI hypotheses under analysis also include a complex phase.

Therefore, in this paper, we present a comprehensive and detailed roadmap for assessing DUNE's capabilities to distinguish among BSO hypotheses, if present in nature, as well as between BSO hypotheses and SO. Equally important to model separation is mapping these comparisons to display the potential distortion between the true  $\delta_{CP}$  and the fitted  $\delta_{CP}$ . The significance of our analysis becomes evident, given that the measurement of  $\delta_{CP}$  will be a pivotal achievement in neutrino physics in the coming years.

## VI. ACKNOWLEDGEMENTS

This work is supported by Huiracocha Scholarship 2020 and *Dirección de Fomento de la Investigación* at Pontificia Universidad Católica del Perú, through Grants No. DFI-2021-0758 and CONCYTEC through Grant No.060-2021-FONDECYT.

- 
- [1] B. T. Cleveland, T. Daily, R. Davis, Jr., J. R. Distel, K. Lande, C. K. Lee, P. S. Wildenhain, and J. Ullman, "Measurement of the solar electron neutrino flux with the Homestake chlorine detector," *Astrophys. J.* **496** (1998) 505–526.
  - [2] **SAGE** Collaboration, J. N. Abdurashitov *et al.*, "Measurement of the solar neutrino capture rate with gallium metal," *Phys. Rev. C* **60** (1999) 055801, [arXiv:astro-ph/9907113](#).
  - [3] **Super-Kamiokande** Collaboration, S. Fukuda *et al.*, "Solar B-8 and hep neutrino measurements from 1258 days of Super-Kamiokande data," *Phys. Rev. Lett.* **86** (2001) 5651–5655, [arXiv:hep-ex/0103032](#).
  - [4] **SNO** Collaboration, Q. R. Ahmad *et al.*, "Direct evidence for neutrino flavor transformation from neutral current interactions in the Sudbury Neutrino Observatory," *Phys. Rev. Lett.* **89** (2002) 011301, [arXiv:nucl-ex/0204008](#).
  - [5] **Super-Kamiokande** Collaboration, Y. Fukuda *et al.*, "Evidence for oscillation of atmospheric neutrinos," *Phys. Rev. Lett.* **81** (1998) 1562–1567, [arXiv:hep-ex/9807003](#).
  - [6] **Super-Kamiokande** Collaboration, T. Kajita, E. Kearns, and M. Shiozawa, "Establishing atmospheric neutrino oscillations with Super-Kamiokande," *Nucl. Phys. B* **908** (2016) 14–29.

- [7] **KamLAND** Collaboration, T. Araki *et al.*, “Measurement of neutrino oscillation with KamLAND: Evidence of spectral distortion,” *Phys. Rev. Lett.* **94** (2005) 081801, [arXiv:hep-ex/0406035](#).
- [8] **MINOS** Collaboration, P. Adamson *et al.*, “A Study of Muon Neutrino Disappearance Using the Fermilab Main Injector Neutrino Beam,” *Phys. Rev. D* **77** (2008) 072002, [arXiv:0711.0769 \[hep-ex\]](#).
- [9] **MINOS** Collaboration, P. Adamson *et al.*, “Measurement of Neutrino and Antineutrino Oscillations Using Beam and Atmospheric Data in MINOS,” *Phys. Rev. Lett.* **110** no. 25, (2013) 251801, [arXiv:1304.6335 \[hep-ex\]](#).
- [10] M. Gasperini, “Testing the Principle of Equivalence with Neutrino Oscillations,” *Phys. Rev. D* **38** (1988) 2635–2637.
- [11] J. T. Pantaleone, A. Halprin, and C. N. Leung, “Neutrino mixing due to a violation of the equivalence principle,” *Phys. Rev. D* **47** (1993) R4199–R4202, [arXiv:hep-ph/9211214](#).
- [12] J. W. F. Valle, “Resonant Oscillations of Massless Neutrinos in Matter,” *Phys. Lett. B* **199** (1987) 432–436.
- [13] M. M. Guzzo, A. Masiero, and S. T. Petcov, “On the MSW effect with massless neutrinos and no mixing in the vacuum,” *Phys. Lett. B* **260** (1991) 154–160.
- [14] G. B. Gelmini and J. W. F. Valle, “Fast Invisible Neutrino Decays,” *Phys. Lett. B* **142** (1984) 181–187.
- [15] J. Schechter and J. W. F. Valle, “Neutrino Decay and Spontaneous Violation of Lepton Number,” *Phys. Rev. D* **25** (1982) 774.
- [16] F. Benatti and R. Floreanini, “Open system approach to neutrino oscillations,” *JHEP* **02** (2000) 032, [arXiv:hep-ph/0002221](#).
- [17] F. Benatti and R. Floreanini, “Massless neutrino oscillations,” *Phys. Rev. D* **64** (2001) 085015, [arXiv:hep-ph/0105303](#).
- [18] V. D. Barger, S. Pakvasa, T. J. Weiler, and K. Whisnant, “CPT odd resonances in neutrino oscillations,” *Phys. Rev. Lett.* **85** (2000) 5055–5058, [arXiv:hep-ph/0005197](#).
- [19] R. Barbieri, P. Creminelli, and A. Strumia, “Neutrino oscillations from large extra dimensions,” *Nucl. Phys. B* **585** (2000) 28–44, [arXiv:hep-ph/0002199](#).
- [20] V. A. Kostelecky, “Neutrino oscillations and Lorentz violation,” in *3rd International Symposium on Quantum Theory and Symmetries*, pp. 707–721. 3, 2004. [arXiv:hep-ph/0403088](#).
- [21] Z. G. Berezhiani, G. Fiorentini, A. Rossi, and M. Moretti, “Neutrino decay solution of the solar neutrino problem revisited,” *JETP Lett.* **55** (1992) 151–156.
- [22] A. M. Gago, H. Nunokawa, and R. Zukanovich Funchal, “The Solar neutrino problem and gravitationally induced long wavelength neutrino oscillation,” *Phys. Rev. Lett.* **84** (2000) 4035–4038, [arXiv:hep-ph/9909250](#).
- [23] M. C. Gonzalez-Garcia, M. M. Guzzo, P. I. Krastev, H. Nunokawa, O. L. G. Peres, V. Pleitez, J. W. F. Valle, and R. Zukanovich Funchal, “Atmospheric neutrino observations and flavor changing interactions,” *Phys. Rev. Lett.* **82** (1999) 3202–3205, [arXiv:hep-ph/9809531](#).
- [24] V. D. Barger, J. G. Learned, P. Lipari, M. Lusignoli, S. Pakvasa, and T. J. Weiler, “Neutrino decay and atmospheric neutrinos,” *Phys. Lett. B* **462** (1999) 109–114, [arXiv:hep-ph/9907421](#).
- [25] E. Lisi, A. Marrone, and D. Montanino, “Probing possible decoherence effects in atmospheric neutrino oscillations,” *Phys. Rev. Lett.* **85** (2000) 1166–1169, [arXiv:hep-ph/0002053](#).
- [26] **Hyper-Kamiokande Proto-** Collaboration, K. Abe *et al.*, “Physics potential of a long-baseline neutrino oscillation experiment using a J-PARC neutrino beam and Hyper-Kamiokande,” *PTEP* **2015** (2015) 053C02, [arXiv:1502.05199 \[hep-ex\]](#).
- [27] **DUNE** Collaboration, B. Abi *et al.*, “Deep Underground Neutrino Experiment (DUNE), Far Detector Technical Design Report, Volume I Introduction to DUNE,” *JINST* **15** no. 08, (2020) T08008, [arXiv:2002.02967 \[physics.ins-det\]](#).
- [28] **DUNE** Collaboration, B. Abi *et al.*, “Deep Underground Neutrino Experiment (DUNE), Far Detector Technical Design Report, Volume II: DUNE Physics,” [arXiv:2002.03005 \[hep-ex\]](#).
- [29] F. D. Díaz, J. Hoefken, and A. M. Gago, “Effects of the violation of the equivalence principle at DUNE,” *Phys. Rev. D* **102** no. 5, (2020) 055020, [arXiv:2003.13712v2 \[hep-ph\]](#).
- [30] P. Coloma, “Non-standard interactions in propagation at the Deep Underground Neutrino Experiment,” *JHEP* **03** (2016) 016, [arXiv:1511.06357 \[hep-ph\]](#).



- [31] M. Masud and P. Mehta, “Nonstandard interactions spoiling the CP violation sensitivity at DUNE and other long baseline experiments,” *Phys. Rev. D* **94** (2016) 013014, [arXiv:1603.01380 \[hep-ph\]](#).
- [32] S. Choubey, S. Goswami, and D. Pramanik, “A study of invisible neutrino decay at DUNE and its effects on  $\theta_{23}$  measurement,” *JHEP* **02** (2018) 055, [arXiv:1705.05820 \[hep-ph\]](#).
- [33] P. Coloma and O. L. G. Peres, “Visible neutrino decay at DUNE,” [arXiv:1705.03599 \[hep-ph\]](#).
- [34] M. Ascencio-Sosa, A. Calatayud-Cadenillas, A. Gago, and J. Jones-Pérez, “Matter effects in neutrino visible decay at future long-baseline experiments,” *Eur. Phys. J. C* **78** (2018) 809, [arXiv:1805.03279v2 \[hep-ph\]](#).
- [35] G. Balieiro Gomes, D. V. Forero, M. M. Guzzo, P. C. De Holanda, and R. L. N. Oliveira, “Quantum Decoherence Effects in Neutrino Oscillations at DUNE,” *Phys. Rev. D* **100** no. 5, (2019) 055023, [arXiv:1805.09818 \[hep-ph\]](#).
- [36] J. A. Carpio, E. Massoni, and A. M. Gago, “Testing quantum decoherence at DUNE,” *Phys. Rev. D* **100** no. 1, (2019) 015035, [arXiv:1811.07923 \[hep-ph\]](#).
- [37] G. Barenboim, A. Calatayud-Cadenillas, A. Gago, and C. Ternes, “Quantum decoherence effects on precision measurements at dune and t2hk,” *Physics Letters B* **852** (2024) 138626. <https://www.sciencedirect.com/science/article/pii/S0370269324001849>.
- [38] G. Barenboim, C. A. Ternes, and M. Tórtola, “Neutrinos, DUNE and the world best bound on CPT invariance,” *Phys. Lett. B* **780** (2018) 631–637, [arXiv:1712.01714 \[hep-ph\]](#).
- [39] A. M. Gago, M. M. Guzzo, H. Nunokawa, W. J. C. Teves, and R. Z. Funchal, “Probing flavor changing neutrino interactions using neutrino beams from a muon storage ring,” *Phys. Rev. D* **64** (Aug, 2001) 073003, [arXiv:hep-ph/0105196 \[hep-ph\]](#). <https://link.aps.org/doi/10.1103/PhysRevD.64.073003>.
- [40] A. M. Gago, H. Minakata, H. Nunokawa, S. Uchinami, and R. Z. Funchal, “Resolving cp violation by standard and nonstandard interactions and parameter degeneracy in neutrino oscillations,” *JHEP* **2010** (2010) 01, [arXiv:0904.3360 \[hep-ph\]](#).
- [41] T. Ohlsson, “Status of non-standard neutrino interactions,” *Rept. Prog. Phys.* **76** (2013) 044201, [arXiv:1209.2710 \[hep-ph\]](#).
- [42] P. Coloma, M. C. Gonzalez-Garcia, M. Maltoni, J. a. P. Pinheiro, and S. Urrea, “Global constraints on non-standard neutrino interactions with quarks and electrons,” *JHEP* **08** (2023) 032, [arXiv:2305.07698 \[hep-ph\]](#).
- [43] G. Barenboim, N. E. Mavromatos, S. Sarkar, and A. Waldron-Lauda, “Quantum decoherence and neutrino data,” *Nucl. Phys. B* **758** (2006) 90–111, [arXiv:hep-ph/0603028](#).
- [44] N. E. Mavromatos, “CPT violation and decoherence in quantum gravity,” *Lect. Notes Phys.* **669** (2005) 245–320, [arXiv:gr-qc/0407005](#).
- [45] J. C. Carrasco, F. N. Díaz, and A. M. Gago, “Probing CPT breaking induced by quantum decoherence at DUNE,” *Phys. Rev. D* **99** no. 7, (2019) 075022, [arXiv:1811.04982 \[hep-ph\]](#).
- [46] A. Capolupo, S. M. Giampaolo, and G. Lambiase, “Decoherence in neutrino oscillations, neutrino nature and CPT violation,” *Phys. Lett. B* **792** (2019) 298–303, [arXiv:1807.07823 \[hep-ph\]](#).
- [47] L. Buoninfante, A. Capolupo, S. M. Giampaolo, and G. Lambiase, “Revealing neutrino nature and CPT violation with decoherence effects,” *Eur. Phys. J. C* **80** no. 11, (2020) 1009, [arXiv:2001.07580 \[hep-ph\]](#).
- [48] J. C. Carrasco-Martínez, F. N. Díaz, and A. M. Gago, “Uncovering the Majorana nature through a precision measurement of the CP phase,” *Phys. Rev. D* **105** no. 3, (2022) 035010, [arXiv:2011.01254 \[hep-ph\]](#).
- [49] J. Carpio, E. Massoni, and A. M. Gago, “Revisiting quantum decoherence for neutrino oscillations in matter with constant density,” *Phys. Rev. D* **97** no. 11, (2018) 115017, [arXiv:1711.03680 \[hep-ph\]](#).
- [50] R. A. Gomes, A. L. Gomes, and O. L. Peres, “Quantum decoherence and relaxation in long-baseline neutrino data,” *JHEP* **10** (2023) 035, [arXiv:2001.09250v4 \[hep-ph\]](#).
- [51] U. Rahaman, “Looking for Lorentz invariance violation (LIV) in the latest long baseline accelerator neutrino oscillation data,” *Eur. Phys. J. C* **81** (2021) 792, [arXiv:2103.04576v2 \[hep-ph\]](#).
- [52] R. A. Gomes, A. L. Gomes, and O. L. Peres, “Constraints on neutrino decay lifetime using long-baseline charged and neutral current data,” *Phys. Lett. B* **740** (2015) 345–352, [arXiv:1407.5640v3 \[hep-ph\]](#).
- [53] A. M. Gago, R. A. Gomes, A. L. Gomes, J. Jones-Pérez, and O. L. Peres, “Visible neutrino decay in the light of appearance and disappearance long-baseline experiments,” *JHEP* **11** (2017) 022,

- [arXiv:1705.03074v2 \[hep-ph\]](#).
- [54] **NOvA** Collaboration, M. A. Acero *et al.*, “Improved measurement of neutrino oscillation parameters by the NOvA experiment,” *Phys. Rev. D* **106** no. 3, (2022) 032004, [arXiv:2108.08219 \[hep-ex\]](#).
  - [55] **NOvA, R. Group** Collaboration, M. A. Acero *et al.*, “Expanding neutrino oscillation parameter measurements in NOvA using a Bayesian approach,” [arXiv:2311.07835 \[hep-ex\]](#).
  - [56] C. Argüelles, J. Salvado, and C. N. Weaver, “A Simple Quantum Integro-Differential Solver (SQuIDS),” *Comput. Phys. Commun.* **196** (2015) 569–591, [arXiv:1412.3832 \[hep-ph\]](#).
  - [57] P. F. de Salas, D. V. Forero, S. Gariazzo, P. Martínez-Miravé, O. Mena, C. A. Ternes, M. Tórtola, and J. W. F. Valle, “2020 global reassessment of the neutrino oscillation picture,” *JHEP* **02** (2021) 071, [arXiv:2006.11237 \[hep-ph\]](#).
  - [58] S. S. Chatterjee and A. Palazzo, “Nonstandard neutrino interactions as a solution to the NO $\nu$ A and t2k discrepancy,” *Phys. Rev. Lett.* **126** (Feb, 2021) 051802.  
<https://link.aps.org/doi/10.1103/PhysRevLett.126.051802>.
  - [59] P. B. Denton, J. Gehrlein, and R. Pestes, “*cp*-violating neutrino nonstandard interactions in long-baseline-accelerator data,” *Phys. Rev. Lett.* **126** (Feb, 2021) 051801.  
<https://link.aps.org/doi/10.1103/PhysRevLett.126.051801>.
  - [60] **DUNE** Collaboration, B. Abi *et al.*, “Experiment Simulation Configurations Approximating DUNE TDR,” [arXiv:2103.04797v2 \[hep-ex\]](#).